International Journal of Mass Spectrometry 308 (2011) 316–329

Contents lists available at SciVerse ScienceDirect

International Journal of Mass Spectrometry

journal homepage: www.elsevier.com/locate/ijms

IR spectroscopy of isolated metal–organic complexes of biocatalytic interest: Evidence for coordination number four for Zn^{2+}(imidazole)$_4$

Anita Lagutschenkov[a], Ulrich Joseph Lorenz[b], Otto Dopfer[a,*]

[a] Institut für Optik und Atomare Physik, Technische Universität Berlin, Hardenbergstrasse 36, 10623 Berlin, Germany
[b] Laboratoire de Chimie Physique Moléculaire, École Polytechnique Fédérale de Lausanne, CH-1015 Lausanne, Switzerland

ARTICLE INFO

Article history:
Available online 27 August 2011

Keywords:
Metal–ligand complexes
Zn^{2+}
Imidazole
IR spectroscopy
Structure elucidation
Zinc enzyme model

ABSTRACT

The characterization of the interactions of Zn^{2+} ions with imidazole ligands is vital for understanding the function of a plethora of zinc enzymes at the molecular level. The infrared multiple photon dissociation (IRMPD) spectrum of mass selected Zn^{2+}(imidazole)$_4$ cations, $[ZnIm_4]^{2+}$, was obtained in the 670–1840 cm^{-1} fingerprint range by coupling the infrared free electron laser (IR-FEL) at the Centre Laser Infrarouge d'Orsay (CLIO) with a quadrupole ion trap mass spectrometer equipped with an electrospray ionization (ESI) source. The experimental efforts are complemented by quantum chemical calculations for $[ZnIm_n]^{2+}$ with n = 1–4 at the B3LYP level using basis sets ranging from cc-pVDZ to aug-cc-pVTZ. By comparison with calculated linear absorption spectra, the transitions observed in the IRMPD spectrum are assigned to vibrational modes of the imidazole ligands. In combination, the experimental data and the calculations provide detailed information about structure, metal–ligand bonding, charge distribution, and binding energy of the $[ZnIm_4]^{2+}$ complex in the gas phase. The superior abundance of the n = 4 complex of $[ZnIm_n]^{2+}$ in the mass spectra of the ESI source is indicative of the preferred coordination number CN = 4 for Zn^{2+} interacting with imidazole ligands in both the gas and the liquid phase. Comparison of the IR spectra of $[ZnIm_n]^{2+}$ with that of bare Im reveals the impact of the strong Zn^{2+}–Im interaction on the electronic, geometric, and vibrational structure of the aromatic ligands upon sequential filling of the first coordination shell. Comparison with the structural and vibrational properties of the imidazole cation demonstrates that the metal-to-ligand charge transfer in $[ZnIm_n]^{2+}$ is dominated by σ donation, whereas contributions from π donation are minor.

1. Introduction

The metal–ligand interactions in complexes of the doubly charged Zn^{2+} ion with four imidazole ligands $[ZnIm_4]^{2+}$ (Fig. 1), have been characterized by infrared (IR) spectroscopy, mass spectrometry, and quantum chemical calculations. Zn^{2+} ions are key structural components in a large number of metalloproteins. Of particular relevance are active centers in enzymes, in which Zn^{2+} coordinates with one or more imidazole (Im) residues of the amino acid histidine (His) [1–9]. The divalent Zn^{2+} ion has the electronic configuration $[Ar]3d^{10}4s^2$, which gives rise to important consequences for its interaction with surrounding ligands [7]. As the $3d^{10}$ shell is completely filled, Zn^{2+} does not exhibit any particular ligand field stabilization effects. As a consequence, the coordination of Zn^{2+} is mainly controlled by the ligand type, size, and interaction energy. Nearly all zinc enzymes feature interactions between Zn^{2+} and the basic N atoms of the Im moiety in the side chain of one or more His ligands, and the coordination number (CN) may readily vary between 4 and 6 [6]. In fact, it is thought that this flexibility in the coordination structure of Zn^{2+} is vital for the function of the large variety of zinc proteins. The Zn^{2+} ion is not redox active, i.e., neither Zn^+ nor Zn^{3+} are available under physiological conditions. Frequently, one or more of the His ligands in metalloproteins are replaced by H_2O, as for example in the fundamental carbonic anhydrase enzyme [2,4–7], which catalyses the reversible formation of HCO_3^- and H^+ from H_2O and CO_2. In order to understand these biocatalytic processes at the molecular level, the relevant metal–ligand interactions present at the active centers have to be characterized in detail [10–13]. To this end, we have started a program to investigate the structure and bonding in isolated complexes of the type $Zn^{2+}(L_1)_n(L_2)_m$ with $L_{1,2}$ = Im, His, and H_2O in the gas phase by IR spectroscopy and quantum chemical calculations [14]. Here, we present a detailed account of the initial results obtained for $[ZnIm_4]^{2+}$.

Recent pioneering efforts by Peschke et al. to explore the mechanism of carbonic anhydrase at the molecular level in the gas phase involve quantum chemical calculations and mass spectrometric studies for the Zn^{2+}/Im/H_2O cluster system [10]. The active

* Corresponding author. Fax: +49 30 31423018.
E-mail address: dopfer@physik.tu-berlin.de (O. Dopfer).

1387-3806/$ – see front matter © 2011 Elsevier B.V. All rights reserved.
doi:10.1016/j.ijms.2011.08.019

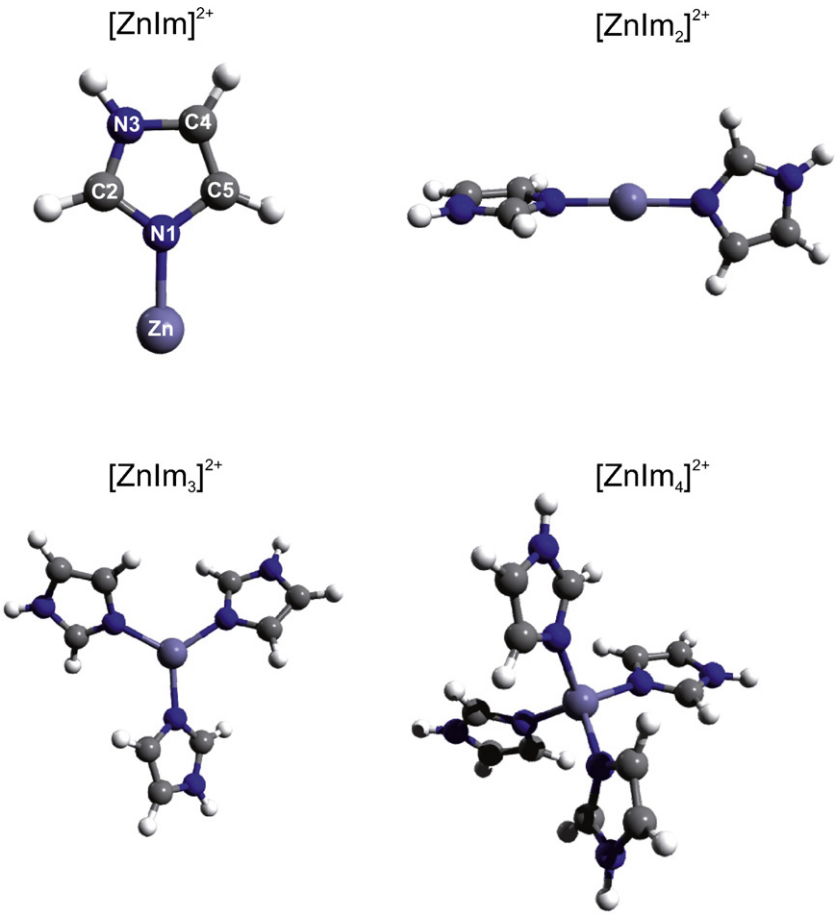

Fig. 1. Selected minimum structures of $[ZnIm_n]^{2+}$ with $n = 1–4$ calculated at the B3LYP/cc-pVTZ level.

center of this enzyme features a Zn^{2+} ion coordinated by three His and one H_2O ligand in a tetrahedral-like configuration. For the purpose of modeling the active center, the His moiety is often replaced by its Im residue in modeling the active center. Although the work by Peschke et al. [10] did not include $[ZnIm_4]^{2+}$, density functional calculations at the B3LYP/6-311G++(d,p) level reveal strongly decreasing incremental ligand binding energies of 761, 536, and 272 kJ/mol for $[ZnIm_n]^{2+}$ with $n = 1–3$. The high binding energies in $[ZnIm_4]^{2+}$ with $n \leq 4$ prevent their experimental determination via standard ion-ligand equilibrium measurements [10]. On the other hand, the free binding energy of the fourth H_2O ligand to $[ZnIm_3]^{2+}$ was measured to be relatively small, $\Delta G = 59$ kJ/mol [10]. It was proposed that it is the strong bonding to three Im (or His) residues that makes (i) Zn^{2+} stable in the enzyme relative to the aqueous environment and (ii) the fourth H_2O ligand only weakly bonded to the Zn^{2+} ion. These two conditions are concluded to be a very favorable precondition for the enzymatic process involving the following accepted mechanism in carbonic anhydrase [4–6]:

$$[ZnHis_3(H_2O)]^{2+} \rightarrow [ZnOHHis_3]^{+} + H^{+} \quad (1)$$

$$[ZnOHHis_3]^{+} + CO_2 + H_2O \rightarrow [ZnHis_3(H_2O)]^{2+} + HCO_3^{-} \quad (2)$$

In this scenario, the His ligands remain bonded to the Zn^{2+} ion, whereas CO_2 and H_2O are converted into HCO_3^- and H^+. A later mass spectrometric study of $[ZnOHIm_n]^+$ supports this type of catalytic reaction mechanism for CO_2 activation [12]. It is the purpose of our IR spectroscopic program [14] to furnish experimental data on the details of the interaction potential in the fundamental Zn^{2+}/His(Im)/H_2O and Zn^{2+}/His(Im)/OH^- cluster systems, which are vital for the understanding of active centers of a variety of Zn enzymes at the molecular level.

A plethora of quantum chemical studies have elucidated the bonding of Zn^{2+} to simple ligands such as $L = H_2O$ and NH_3 [10,15–22]. These studies reveal that the flexibility in the CN in $[ZnL_n]^{2+}$ arises from a subtle competition of mainly three effects, namely electronic, electrostatic, and steric interaction [22]. Electronically, the 18 electron counting rule favors CN = 4 of Zn^{2+} (10 d electrons) interacting with 4 ligands donating each 2 σ electrons. Electrostatically, the strong charge–dipole attraction tends to maximize the number of ligands in the first coordination shell, which will eventually be limited by steric hindrance arising from ligand–ligand repulsion. Quantum chemical calculations predict similar stabilities for isomeric $[Zn(H_2O)_n]^{2+}$ clusters with coordination numbers between 4 and 6 and low barriers for their interconversion [17,18,22]. The relative stability of the isomers depends somewhat on the theoretical level [18] and also on temperature because entropy may change their energetic order [17]. Mass spectrometric and spectroscopic studies on small $[Zn(H_2O)_n]^{2+}$ clusters are hampered by the competing charge-separation reaction, which implies that usually only clusters with $n \geq 7$ are generated in electrospray ionization (ESI) sources [20–22]. Very recent IR spectra of $[Zn(H_2O)_n]^{2+}$ with $n = 6–12$ in the O–H stretch range are consistent with a predominant CN of 5, with a minor contribution from isomers with CN = 6 [22].

Experimental information on the structures and binding energies of isolated $[ZnIm_n]^{2+}$ ions is not available. As already mentioned, standard mass spectrometric techniques are not suitable to establish binding energies for such strongly bound, doubly charged cluster ions [10]. ESI mass spectra of solutions containing

$ZnCl_2$ (or other ZnX_2 salts) and Im exhibit the pronounced formation of $[ZnIm_4]^{2+}$, suggesting that the preferred coordination number of $[ZnIm_n]^{2+}$ is CN = 4 [10,12], although it was not specified whether this preference holds for the solution and/or the gas phase. Quantum chemical calculations for $[ZnIm_n]^{2+}$ at the MP2 (n = 1) [15,23] and B3LYP level (n = 1–3) [10,23,24] yield information about the structure, interaction energy, and metal-to-ligand charge transfer. For example, the incremental ligand bond energies calculated at the B3LYP/6-311++G(d,p) level decrease significantly and rather monotonically as n increases (761, 536, and 272 kJ/mol for n = 1–3 [10]). Calculations and mass spectrometric studies for the related isoelectronic singly charged $[CuIm_n]^+$ cluster series ($n \leq 4$) demonstrate that the interaction is much weaker in the Cu^+ clusters as compared to the Zn^{2+} species [25,26]. Moreover, the type of bonding is also different, as evident from the measured incremental ligand binding energies [25], which exhibit a sharp drop after n = 2 (288, 258, 80, and 64 kJ/mol for n = 1–4). Interestingly, density functional theory calculations and mass spectrometric studies suggest that the most stable isomers of $[CuIm_n]^+$ with $n \geq 3$ are composed of a $[CuIm_2]^+$ trimer core (i.e., CN = 2), with further Im ligands being hydrogen-bonded to the acidic NH protons of the two ligands in the first coordination shell [25]. This difference between Cu^+ and Zn^{2+} may not only be attributed to their different charge but also to their different tendency for sd hybridization [27].

Early IR spectra of $[ZnIm_n]^{2+}$ ions (n = 4–6) in crystalline salts with a variety of counter anions provide information about the structure and bonding of the ion core in the condensed phase [1,28–31]. The vibrational assignment of these spectra suggests that the coordination symmetry of the $[ZnIm_n]^{2+}$ cations in these salts varies from tetrahedral for n = 4 to square-based pyramidal for n = 5 and octahedral for n = 6, again demonstrating the ability of the Zn^{2+} ion to readily change the CN between 4 and 6 [28]. In particular, the Zn–N stretch vibration occurring in the 200–400 cm^{-1} spectral range of the FIR spectrum was shown to be a sensitive probe of the coordination structure and the Zn–N bond strength [28–30]. Although these crystal spectra provide detailed insight into the geometric structure and the metal-to-ligand bond strength of the $[ZnIm_n]^{2+}$ ions in the solid phase, some of the vibrational frequencies are largely perturbed by the presence of counter anions, which also severely modify relevant parts of the IR spectrum via their own vibrational absorptions [28].

In recent years, the fruitful combination of IR spectroscopy, mass spectrometry, and quantum chemistry has proven to be an efficient tool to access details of the interaction potential energy surface in metal–organic complexes isolated in the gas phase, such as their structure and binding energy [32–39]. In particular, electrospray ionization has frequently been employed as a convenient ion source for the generation of a large variety of metal–organic complexes. The most sensitive strategy for IR spectroscopy of mass-selected ions and cluster ions relies on IR photodissociation (IRPD) techniques conducted in various types of tandem mass spectrometers [33,34,40–52]. For strongly bound metal–organic cluster ions, the absorption of multiple IR photons is frequently required to induce dissociation, and the necessary high IR laser power to drive such an IR multiple photodissociation (IRMPD) process is readily provided by tunable IR free electron lasers (IR-FEL) [37,53,54]. In the past decade, the application of IRMPD of ESI-generated organic and metal–organic complexes using IR-FEL lasers has developed into a routine strategy, and the reader is referred to several review articles for recent activities in this field [36,52,54–58]. Recent applications from our group include several metal–organic complexes, such as $[Ag–phenol]^+$ [59], $[Ag–(pyridine)_2]^+$ [60], $[Ag–PAH]^+$ with PAH = azulene, naphthalene, anthracene, phenanthrene, and pyrene [61], and $[ZrOH(C_5H_5)_2CH_3CN]^+$ [62], as well as a variety of protonated aromatic molecules [44,63–65] and neurotransmitters [66–68]. IRMPD spectroscopic studies of Zn-bearing ions include $[Zn–(phenylalanine–H)]^+$ [69] and Zn^{2+} complexes of a variety of crown ethers [70]. In addition, the IRMPD spectrum of Im-Fe^+-heme was reported, although the metal–Im interaction in the complex was not considered [71].

The present work reports the IRMPD spectrum of ESI-generated $[ZnIm_4]^{2+}$ ions in the informative fingerprint range. Significantly, this spectrum yields for the first time experimental information about the Zn^{2+}–Im interaction in these biochemically relevant species in the gas phase. Moreover, the systematic quantum chemical characterization of $[ZnIm_n]^{2+}$ complexes with n = 1–4 at the density functional theory level provides insight into the evolution of the metal–ligand interaction as a function of the number of ligands in the first coordination shell (Fig. 1). Comparison of the properties of $[ZnIm_n]^{2+}$ with those of isolated Im [72–74] provides details about the effects of Zn^{2+} complexation and the accompanying charge transfer on the geometrical parameters of the ligands, which can directly be monitored in the IR spectrum. Comparison of $[ZnIm_n]^{2+}$ with the imidazole radical cation (Im^+ [75–79]) and the protonated molecule (ImH^+ [76,80]) elucidates the predominant mechanism for charge transfer (σ vs. π donation).

2. Experimental and theoretical techniques

IRMPD spectra of mass-selected $[ZnIm_4]^{2+}$ ions were obtained in a modified Bruker Esquire 3000 quadrupole ion trap mass spectrometer coupled to the IR-FEL at CLIO [81]. This experimental strategy has been described in detail elsewhere [81]. Briefly, the IR-FEL is based on a linear electron accelerator, and the range of the tunable IR frequency depends on the electron kinetic energy, which can be varied between 10 and 50 MeV [82]. The FEL was operated at 45 and 36 MeV to cover the spectral range between 670 and 1840 cm^{-1}. The IR-FEL output consists of 8 μs long macropulses emitted at a repetition rate of 25 Hz. Each macropulse is composed of 500 micropulses, each a few ps long and separated by 16 ns. For the typical IR average power of 500 mW used in the present work, the corresponding micropulse and macropulse energies are 40 μJ and 20 mJ, respectively. The laser wavelength was calibrated using a monochromator coupled to a pyroelectric detector array. The IR-FEL spectral width (FWHM) was less than 0.5% of the central wavelength. A spherical mirror with 1 m focal length was used to mildly focus the IR-FEL beam at the center of the ion trap, and its position was adjusted by optimizing the fragmentation efficiency. The IR laser beam accessed the center of the ion trap through a ZnSe window and a conical hole in the ring electrode.

$[ZnIm_4]^{2+}$ ions were produced by ESI of a methanol/water solution (20:1) containing $ZnCl_2$ (75 μM) and imidazole (75 μM). Multistage mass spectrometry was carried out using the standard Bruker Esquire Control software (version 5.2). The first step ensured proper mass selection of the ions of interest. In a subsequent step, the mass selected ions were assayed either by collision-induced dissociation (CID) or by IRMPD, and the resulting fragments were analyzed after the interaction time. IRMPD of $[ZnIm_4]^{2+}$ was accomplished by exposing mass-selected ions to 6 macropulses of the IR-FEL and averaging typically 20–40 mass spectra at each wavelength, which was varied in steps of 2–4 cm^{-1} depending on the wavelength. When the laser is resonant with a vibrational transition, the ion absorbs incoherently multiple photons in a stepwise process until the (lowest) dissociation threshold is reached. By monitoring the intensities of parent (I_P) and resulting fragment ions (I_F) as a function of the laser wavenumber, the IRMPD yield is obtained as $-\ln(I_P/[I_P + \sum I_F])$. Only the monoisotopic species of $[ZnIm_4]^{2+}$ (m = 278.0122 u) has been investigated. Despite its multiple photonic nature, the IRMPD spectrum predominantly reflects the resonant absorption of the first IR photon, and the reader is referred to Ref. [54] for a recent review of the IRMPD mechanism.

This observation justifies a comparison of the experimental IRMPD spectrum with a calculated linear one-photon IR absorption spectrum. There are often minor but noticeable deviations of the IRMPD spectrum of a molecular ion from its linear IR absorption spectrum, including redshifts of vibrational frequencies of up to 30 cm^{-1}, modifications of relative IR intensities of neighboring vibrational transitions, and the lack of observation of transitions with IR cross sections below a certain threshold intensity [54]. These differences between IRMPD and IR spectra are usually more pronounced for ions with higher dissociation energies.

Quantum chemical calculations for Im, Im^+, and $[ZnIm_n]^{2+}$ with $n \leq 4$ were carried out at the B3LYP level using the cc-pVDZ, aug-cc-pVDZ, cc-pVTZ, and aug-cc-pVTZ basis sets [83]. Calculations for $[ZnIm_n]^{2+}$ reveal the dependence of various relevant properties of the complexes on the number of ligands in the first coordination shell, including the Zn^{2+}–Im bond strength, the metal-to-ligand charge transfer, and its impact on the ligand geometry and the appearance of the IR spectrum. For comparison, the properties of Im^+ in its $^2A''$ ground electronic state were also investigated in order to evaluate the effects of charge transfer in the limit of complete ionization of Im. The properties of the strongly bound $[ZnIm_n]^{2+}$ complexes are almost independent of the size of the considered basis sets. For example, the Zn–Im bond energy in $[ZnIm]^{2+}$ amounts to 777.6, 761.6, 766.0, 763.5 kJ/mol using the cc-pVDZ, aug-cc-pVDZ, cc-pVTZ, and aug-cc-pVTZ basis sets, respectively, in good agreement with the value of 761 kJ/mol calculated recently at the B3LYP/6-311++G(d,p) level [10]. Thus, only the data for the cc-pVTZ basis are reported in Tables and Figures. Inclusion of relativistic effects on the Zn^{2+}–Im interaction by using effective core potentials increases the binding energies by merely 3% (~20 kJ/mol). Therefore, all further calculations were carried out without effective core potentials. All coordinates were optimized in the search of minimum structures on the potential energy surface. Reported energies were corrected for harmonic zero point vibrational energies. The considered interaction energies of $[ZnIm_n]^{2+}$ include the total binding energies (D_0) with respect to dissociation into Zn^{2+} and separate Im ligands, and average binding energies obtained as $D_0^a = D_0/n$. Vibrational frequencies for the cc-pVTZ basis were scaled by factors of 0.98 and 0.96 for frequencies below and above 2000 cm^{-1}, respectively [84]. These dual scaling factors optimize the agreement between calculated and measured frequencies of isolated imidazole (Table 1) [72,73]. For ease of comparison with the IRMPD spectrum, theoretical IR stick absorption spectra are convoluted with Gaussian line profiles using FWHM = 15 cm^{-1}. The charge distribution was determined using the natural bond orbital (NBO) analysis.

In order to elucidate the effects of electron correlation on the Zn^{2+}–Im interaction, test calculations were carried out at the MP2/cc-pVTZ level for the $[ZnIm]^{2+}$ dimer ($n = 1$). In agreement with previous observations [10,15], the Zn^{2+}–Im interaction energy at the MP2/cc-pVTZ level (711 kJ/mol) is about 7% lower than the B3LYP/cc-pVTZ value (766 kJ/mol). As no experimental data are available for $[ZnIm]^{2+}$, it is difficult to judge at the present stage which of the two theoretical approaches provides a better description of the Zn^{2+}–Im interaction. As the IR spectrum of $[ZnIm_4]^{2+}$ calculated at the B3LYP/cc-pVTZ level shows satisfactory agreement with the measured IRMPD spectrum (Section 3.3), all calculations of the $[ZnIm_n]^{2+}$ cluster series were conducted at this level. The MP2 calculations were limited to the $n = 1$ species not only due to limits in available computational resources but also because of the well-known difficulty of this theoretical approach to reliably predict several vibrational frequencies of aromatic molecules [60,64,65,85]. On the other hand, B3LYP calculations produced IR spectra in good agreement with experimental spectra for aromatic species [59,60,62–66,68].

3. Results and discussion

3.1. Experimental results

A typical mass spectrum of the ESI source obtained in the positive ion mode is reproduced in Fig. 2. The mass spectrum is dominated by clusters of imidazole, and the most intense peaks at m/z 69 and 137 are readily assigned to ImH^+ and Im_2H^+, respectively. Their large abundance is consistent with the high proton affinity of imidazole (943 kJ/mol [86]) and the large binding energy of the proton-bound dimer (~110 kJ/mol [87]). Efforts to generate longer Im_nH^+ proton-wire clusters [76,88] with $n \geq 3$ in this source failed, probably because of their reduced binding energy. The mass spectrum also displays signals arising from singly and doubly charged complexes containing a single Zn ion, which are readily identified by their characteristic isotopic pattern. No complexes with two Zn ions are observed. Species with ^{64}Zn corresponding to the monoisotopic ions are assigned in the mass spectrum in Fig. 2. Inspection of this mass spectrum reveals the presence of doubly charged clusters of the type $[ZnIm_n]^{2+}$ with $n = 2$–4. Corresponding clusters with $n \leq 1$ and $n \geq 5$ are below the detection limit. The relative abundance of 500:100:1 for $[ZnIm_n]^{2+}$ decreases strongly in the order $n = 4 > 3 > 2$. This observation is indicative of the preferred coordination number CN = 4 for Zn^{2+} ions with Im ligands, in line with previous theoretical and mass spectrometric studies modeling the role of Zn^{2+} ions in enzymatic reactions involving His and H_2O ligands [3,10,12]. This result is in contrast to the isoelectronic $[CuIm_n]^+$ complexes, which prefer cluster structures with CN = 2 [25,26], emphasizing the significant differences between the metal–ligand coordination of Cu^+ and Zn^{2+}. These can mainly be traced back to the vastly different interaction strengths arising from the different charge state. In $[ZnIm_n]^{2+}$, the much larger electrostatic attraction strongly favors coordination in the first shell, while in the less strongly bound $[CuIm_n]^+$ complexes hydrogen-bonding interactions between ligands in the first and second shell can compete with the metal–ligand interaction in the size range $n \geq 3$. Interestingly, the related $[Zn(H_2O)_n]^{2+}$ appear to favor structures with CN = 5 [22], indicating that the ligand size and ligand type are also important factors for the structure of the first coordination shell. The basic N atom in Im is a significantly better σ donor than the O atom of H_2O, so that the dissociation energy of $[ZnIm]^{2+}$ (~760 kJ/mol) is almost twice as high as that of $[Zn(H_2O)]^{2+}$ (390 kJ/mol [17]). Moreover, the larger Im ligand induces stronger ligand–ligand repulsion forces arising from steric hindrance. In addition to $[ZnIm_n]^{2+}$, the mass spectrum displays a variety of singly charged Zn complexes, namely $[Zn(Im–H)Im_{2,3}]^+$, $[ZnOHIm_{1-3}]^+$, and $[ZnOHIm_{2,3}(H_2O)]^+$. The propensity for the formation of high ion yields for $[ZnIm_4]^{2+}$ and Im_2H^+ has been reported previously for ESI of similar solutions [10]. In the latter work, also high intensity of $[ZnOHIm_3(H_2O)]^+$ was observed and it was suggested that this species is formed via the following reaction [10]:

$$[ZnIm_3(H_2O)_n]^{2+} + B \rightarrow [ZnOHIm_3(H_2O)_{n-1}]^+ + BH^+ \text{ (e.g., B = Im)} \quad (3)$$

The $[Zn(Im–H)Im_n]^+$ complexes may be formed in a similar reaction (3) or by charge separation according to reaction (4) described below.

Mass spectra of products derived from collision-induced dissociation (CID) of mass-selected monoisotopic $[ZnIm_4]^{2+}$ ions with m/z 168 were recorded to confirm its composition and to establish the low-energy dissociation processes (Fig. 3). The only primary fragmentation process detected upon CID corresponds to the

Table 1
Experimental vibrational frequencies of $[ZnIm_4]^{2+}$ and Im (in cm^{-1}) compared to frequencies calculated for the $[ZnIm_4]^{2+}$ isomer (Fig. 1) and Im at the B3LYP/cc-pVTZ level.

$[ZnIm_4]^{2+}$ exp[a]	$[ZnIm_4]^{2+}$ calc[b,c]	Δ[f] exp-calc	$ZnIm_4(ClO_4)_2$ exp[k]	Mode	Im calc[b]	Im exp[d]	Im exp[e]	Δ[g] exp	Δ[h] calc
	189 (0)			σ (*a*)					
	255 (91)		271	σ (*t*)					
	616 (99)		614	ν_{20}	636 (9)	637	636		−20
	655 (224)		652	ν_{19}	671 (5)	664	662		−16
690 (16) A	687 (126)	+3	730	ν_{21}	518 (88)	553	551	+139	+169
							538	+152	
770 (18) B	765 (156)	+5	760	ν_{18}	723 (36)	729	735	+35	+42
840 (18) C	838 (65)	+2	833	ν_{17}	807 (31)	811	810	+30	+31
	882 (2)			ν_{16}	862 (4)	852	850	+20	
913 (11) D	919 (19)	+6	920	ν_{14}	928 (2)	927	916	−3	−9
950 (10) E	951 (12)	+1	953	ν_{15}	891 (9)	893	892	+58	+60
970 (11) F									
988 (9) G									
1081 (17) H	1068 (309)	+13	1050	ν_{13}	1053 (38)	1059	1056	+25	+15
1112 (20) I	1108 (51)	+4		ν_{12}	1073 (17)	1076	1074	+41	+35
1120 I[i]	1123 (34)	+3	1133	ν_{10}	1138 (5)	1103	1120	0	+3
1144 (12) J									
1169 (15) K	1175 (36)	−6	1183	ν_{11}	1123 (3)	1124	1130	+39	+52
1258 (16) L	1267 (53)	−11	1267	ν_9	1261 (0)	1256	1252	+6	+6
1289 (16) M				$2\nu_{19}$?					
1318 (17) N	1334 (34)	−16	1331	ν_8	1338 (6)	1333	1325	−7	−4
1425 (10) O	1426 (47)	−1	1431	ν_7	1402 (14)	1407	1404	+21	+24
1474 (16) P				$\nu_{18}+\nu_{21}$?					
1509 (24) Q	1507 (187)	+2	1512	ν_6	1472 (15)	1483	1480	+29	+35
1539 (14) R	1553 (79)	−14	1546	ν_5	1527 (12)	1522	1518	+21	+26
1614 (14) S				$\nu_{17}+\nu_{18}$?					
	3138 (18)		3131	ν_4	3110 (6)	3090			+28
	3140 (56)		3145	ν_3	3113 (0)				+27
	3157 (39)		3160	ν_2	3142 (2)	3114			+15
	3474 (743)		3380	ν_1	3510 (52)	3500	3504		−36

[a] Peak positions, widths (FWHM in parentheses), and labels taken from IRMPD spectrum in Fig. 5.
[b] Frequencies below (above) 2000 cm^{-1} are scaled by 0.98 (0.96). IR intensities in km/mol are given in parentheses.
[c] Average frequency of the four nearly degenerate modes corresponding to the four almost equivalent Im ligands. The IR intensity is the sum of all four modes. The splitting for all intramolecular modes (ν_i with i = 1–21) is below 6 cm^{-1}. Explicit vibrational frequencies and IR intensities of each individual modes are available in Table S1 in Supporting information.
[d] Ref. [73] (Ar matrix).
[e] Ref. [72] (gas phase).
[f] Difference of experimental and calculated frequencies of $[ZnIm_4]^{2+}$.
[g] Difference of experimental frequencies of $[ZnIm_4]^{2+}$ and Im using the values of Ref. [72].
[h] Difference of calculated frequencies of $[ZnIm_4]^{2+}$ and Im.
[i] Shoulder.
[k] Crystal data from Ref. [28].

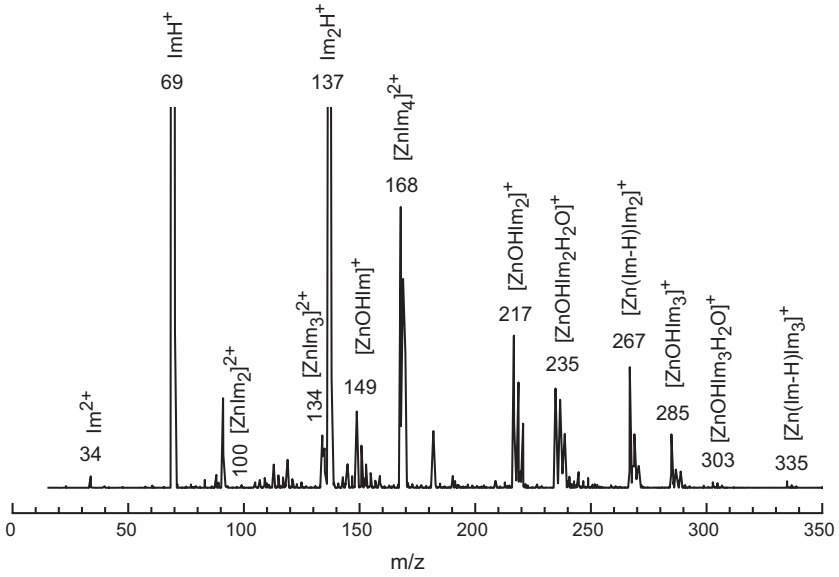

Fig. 2. Mass spectrum of the ESI source measured by analyzing the ion content in the quadrupole ion trap. The saturated peaks attributed to ImH^+ and Im_2H^+ at m/z 69 and 137 are more intense by a factor 15 and 5 than the peak at m/z 168 assigned to $[ZnIm_4]^{2+}$. Assignments are given for the monoisotopic species.

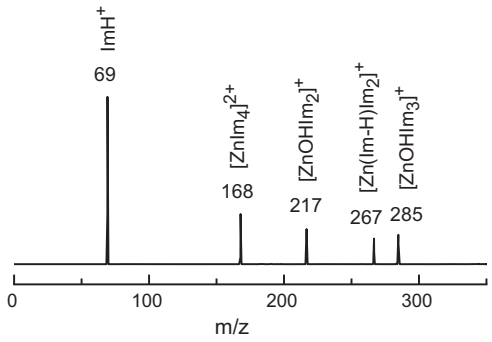

Fig. 3. Mass spectrum obtained from the quadrupole ion trap after initial mass selection of monoisotopic $[ZnIm_4]^{2+}$ with m/z 168 and subsequent collision-induced dissociation. The assignments of the resulting fragmentation and secondary reaction products with H_2O background vapor are indicated.

dissociative charge transfer reaction yielding ImH^+ and $[Zn(Im–H)Im_2]^+$ with m/z 69 and 267:

$$[ZnIm_4]^{2+} \rightarrow ImH^+ + [Zn(Im–H)Im_2]^+ \quad (4)$$

Significantly, fragment ions resulting in the loss of neutral Im ligands were not observed, indicating that the loss of neutral ligands is energetically more demanding than the charge-separation reaction. This situation is often observed for doubly charged ions coordinated by a small number of ligands [21,89,90]. Interestingly, the CID mass spectrum also displays ions with m/z 217 and 285, which are assigned to $[ZnOHIm_2]^+$ and $[ZnOHIm_3]^+$, respectively. These ions are generated in secondary events in the ion trap during the time window of the CID process. These processes involve reactions with abundant H_2O molecules arising from the water background pressure in the trap. The $[ZnOHIm_3]^+$ ions are presumably produced by adduct formation according to

$$[Zn(Im–H)Im_2]^+ + H_2O \rightarrow [ZnOHIm_3]^+ \quad (5)$$

or ligand exchange accompanied by proton transfer according to

$$[ZnIm_4]^{2+} + H_2O \rightarrow [ZnOHIm_3]^+ + ImH^+ \quad (6)$$

The latter mechanism appears less likely because no $[ZnIm_4(H_2O)]^{2+}$ adducts were detected in the mass spectra, consistent with the much weaker bonding of H_2O to Zn^{2+} as compared to Im [10] and the filled first coordination shell in $[ZnIm_4]^{2+}$. The lack of $[ZnIm_4(H_2O)]^{2+}$ ions in these mass spectra provides indeed further evidence for the preferred CN of 4 of $[ZnIm_n]^{2+}$ in the gas phase, which prevents facile attachment of a H_2O ligand to $[ZnIm_4]^{2+}$ in the first shell. The $[ZnOHIm_2]^+$ ions could be formed by "ligand exchange" according to

$$[Zn(Im–H)Im_2]^+ + H_2O \rightarrow [ZnOHIm_2]^+ + Im \quad (7)$$

Several product ions were detected upon IRMPD of mass-selected monoisotopic $[ZnIm_4]^{2+}$ (m/z 168), namely ImH^+, $[ZnOHIm_2]^+$, and $[ZnOHIm_3]^+$ with m/z 69, 217, and 285 (Fig. 4). Similar to the CID experiments, the $[ZnOHIm_n]^+$ species are probably produced from the initial $[Zn(Im–H)Im_2]^+$ photoproduct by secondary reactions with background H_2O in the ion trap before analyzing the content of the ion trap. Interestingly, all primary $[Zn(Im–H)Im_2]^+$ photoproduct ions are depleted by such reactions. In Fig. 4, the action spectra monitored in all major product ion channels are compared to the parent ion signal in the 950–1840 cm^{-1} range available when operating the FEL at 45 MeV. The depletion in the parent channel is 80% for the strongest resonance at ~1070 cm^{-1}, indicating efficient IRMPD. The appearance of the IR action spectra is similar for all three product ions in Fig. 4, although the relative peak intensities seem to slightly depend on the vibrational resonance. The latter observation may indicate that initially

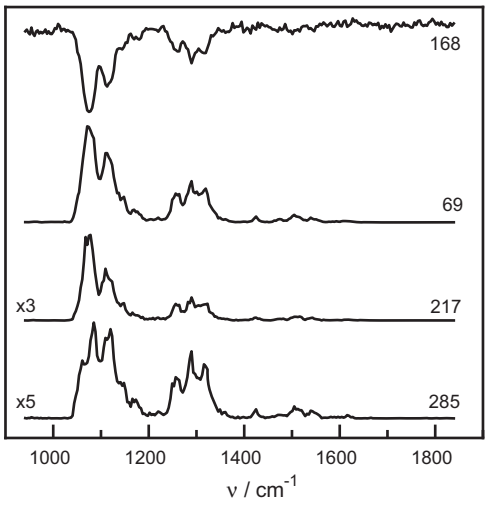

Fig. 4. IR action spectra of mass-selected $[ZnIm_4]^{2+}$ ions monitored in the parent ion channel (m/z 168), as well as in the primary ImH^+ fragment (m/z = 69) and secondary $[ZnOHIm_2]^+$ and $[ZnOHIm_3]^+$ reaction product channels (m/z 217 and 285).

generated photoproducts undergo further resonant IR absorption [65,91]. All three product channels observed are used to derive the total IRMPD yield shown in Fig. 5. In general, the IRMPD yield shows good correspondence with the IR depletion spectrum measured for $[ZnIm_4]^{2+}$ (Fig. 4). However, the IRMPD spectrum displays a better signal-to-noise ratio because it accounts for variations in the parent ion production. Thus, the IRMPD spectrum is used for comparison with calculated spectra.

The IRMPD spectrum in Fig. 5 is composed of two scans in the 670–1300 and 950–1840 cm^{-1} ranges obtained when operating the FEL at 36 and 45 MeV, respectively. The spectra in both ranges were joined at 1030 cm^{-1} in such a way that band H has the same intensity. As the laser power measured for the two wavelength ranges shows only a smooth variation as a function of the laser frequency (Fig. 5), the IRMPD spectrum was not

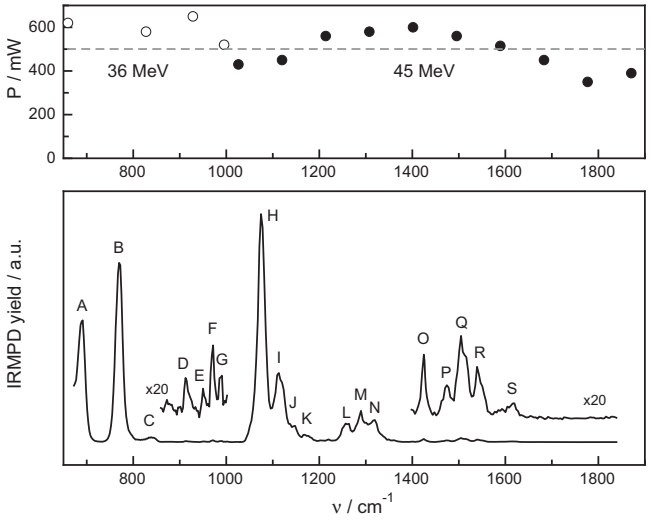

Fig. 5. IRMPD spectrum of mass-selected $[ZnIm_4]^{2+}$ ions in the 670–1840 cm^{-1} fingerprint range (bottom). It is composed of two scans in the 670–1030 and 1030–1840 cm^{-1} ranges obtained when operating the FEL at 36 and 45 MeV, respectively. The positions, widths, and vibrational assignments of the observed peaks (A–S) are listed in Table 1. The IRMPD spectrum is not normalized for laser intensity variations (top), which are plotted as open and filled circles for wavenumbers generated at 36 and 45 MeV, respectively. The dashed line corresponds to P = 500 mW. The intensity of the bands O–R may significantly be reduced due to atmospheric water absorptions in the IR-FEL laser beam path (see text).

normalized for laser intensity variations. In total, 19 bands are extracted from the IRMPD spectrum (denoted A–S), and their positions, widths, and proposed assignments are listed in Table 1. The width of the bands of ~10–20 cm^{-1} arises from several contributions, including (i) the finite laser bandwidth of 0.5% (i.e., 3.5–8 cm^{-1} for ν = 700–1600 cm^{-1}), (ii) unresolved rotational structure of the ions at 300 K in the trap (~5 cm^{-1}), (iii) spectral congestion due to overlapping vibrational resonances and possible contributions from more than one isomer, and (iv) spectral broadening induced by the multiple photonic nature of the IRMPD process [54]. Rotational band contour simulations using the rotational constants of $[ZnIm_4]^{2+}$ calculated at the B3LYP/cc-pVTZ level ($B \sim 0.23$ GHz ~ 0.008 cm^{-1}) suggest that up to 5 cm^{-1} of the observed width may be attributed to unresolved rotational fine structure at 300 K. The most narrow band at 1425 cm^{-1} (band O) has a width of ~10 cm^{-1}, which is close to the width expected from the rotational contour (5 cm^{-1}) and the laser resolution at this frequency (7 cm^{-1}). Despite its multiple photonic nature, the IRMPD spectrum predominantly reflects the absorption of the first IR photon [54] and thus justifies direct comparison with a calculated linear one-photon IR absorption spectrum.

3.2. Quantum chemical results

Calculated minimum structures for Im, Im^+, and $[ZnIm_n]^{2+}$ with n = 1–4 are shown in Figs. 1 and 6, and relevant structural parameters are listed in Table 2 and visualized in Figs. 7 and 8. Relevant parameters of the Zn–Im interaction in $[ZnIm_n]^{2+}$ are compared in Fig. 7, whereas corresponding IR spectra are plotted in Fig. 9. As the experimental spectrum has been obtained only for n = 4, the calculations for Im, Im^+, and $[ZnIm_n]^{2+}$ with $n \leq 4$ have mainly been carried out to establish a general qualitative trend for the evolution of salient properties of the Zn–Im interaction in $[ZnIm_n]^{2+}$ as a function of the degree of coordination (n). The considered parameters include geometrical parameters of the Im ring, the total and average binding energies (D_0, D_0^a), Zn–Im bond lengths (R_{ZnN}), charge delocalization as evaluated by the remaining charge on Zn (q_{Zn}) and the charge on each Im ligand (q_{Im}), and the IR spectrum. For this purpose, only limited parts of the complex potential energy surfaces of $[ZnIm_n]^{2+}$ have been investigated and no efforts of a complete search for all possible isomers have been made. Most of these arise from internal rotation of the Im ligands, which has essentially no impact on the binding energy and the IR spectrum (vide infra). As the mass spectrum strongly suggests that the first coordination shell is closed for n = 4 under the current experimental conditions, calculations have been limited to $[ZnIm_{n\leq4}]^{2+}$ isomers, in which the Im ligands occupy positions in the first coordination shell. With the exception of the n = 1 (C_1, C_s) and n = 2 structures (C_2, C_{2v}), no symmetry restrictions have been applied.

We first discuss the metal–ligand bond properties of the $[ZnIm_n]^{2+}$ complexes. Fig. 6 summarizes the structural parameters calculated for Im, Im^+, and $[ZnIm]^{2+}$ at the B3LYP/cc-pVTZ level (Table 2). In the $[ZnIm]^{2+}$ dimer, the Zn^{2+} ion interacts strongly with the basic N atom of the nearly planar Im ligand, with bond parameters of R_{ZnN} = 1.884 Å and $D_0 = D_0^a$ = 766 kJ/mol (7.94 eV). Interestingly, the complex is slightly nonplanar, with a dihedral angle of θ_{NCNZn} = 6.7°. The Zn–Im stretch frequency amounts to $\sigma = \sigma_{ZnN}$ = 304 cm^{-1}. A substantial part of the positive charge of the Zn^{2+} ion (0.39 e) in $[ZnIm]^{2+}$ is delocalized over the Im ligand. Analysis of the molecular orbitals reveals that the nonbonding lone-pair σ orbital (HOMO-1) of the basic N atom in Im donates electron density to Zn^{2+}, leading to a strong σ-type interaction. An additional weak contribution from the HOMO (π orbital) causes the Zn^{2+} ion to be located slightly out of the aromatic plane (π donation). In fact, the planar $[ZnIm]^{2+}$ structure corresponds to a transition state between two equivalent nonplanar minima with a small barrier

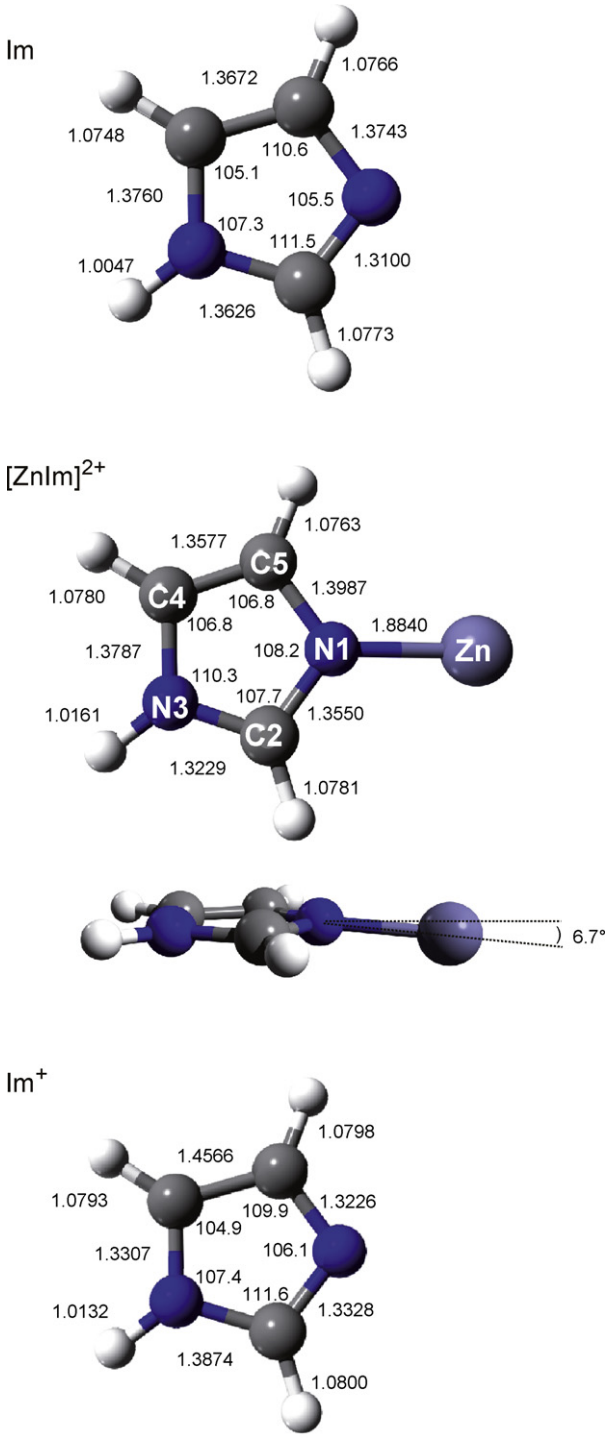

Fig. 6. Structural parameters (in Å and °) of Im, Im^+, and $[ZnIm]^{2+}$ obtained at the B3LYP/cc-pVTZ level (Table 2).

of 33 cm^{-1} (0.4 kJ/mol). This transition state is less stable than the bent minima due to reduced π interactions. Although the binding energy appears to be slightly weaker in the planar structure, the interatomic Zn–N distance is somewhat shorter (R_{ZnN} = 1.874 Å).

The slight deviation from planarity in $[ZnIm_n]^{2+}$ is reproduced by B3LYP calculations employing all four considered basis sets (aug-)cc-pVXZ (X = D, T), with dihedral angles in the range of θ_{NCNZn} = 5.6–8.8° and low barriers to planarity between 20 and 110 cm^{-1}. A potential energy scan along the dihedral angle using the cc-pVDZ basis as well as the analysis of harmonic vibrational

Table 2
Salient structural, energetic, and vibrational parameters of $Im^{(+)}$ and $[ZnIm_n]^{2+}$ complexes with $n = 1–4$ evaluated at the B3LYP/cc-pVTZ and MP2/cc-pVTZ levels (Figs. 1 and 6).

Parameter	Im B3LYP	$[ZnIm]^{2+}$ B3LYP	$[ZnIm_2]^{2+}$ B3LYP	$[ZnIm_3]^{2+}$ B3LYP	$[ZnIm_4]^{2+}$ B3LYP	Im^+ B3LYP	Im MP2	$[ZnIm]^{2+}$ MP2
R_{N1C2} (Å)	1.3100	1.3550	1.3430	1.3333	1.3271	1.3328	1.3216	1.3591
R_{C2N3} (Å)	1.3626	1.3229	1.3285	1.3362	1.3417	1.3874	1.3617	1.3276
R_{N3C4} (Å)	1.3760	1.3787	1.3772	1.3750	1.3740	1.3306	1.3707	1.3712
R_{C4C5} (Å)	1.3672	1.3577	1.3549	1.3581	1.3604	1.4566	1.3765	1.3652
R_{C5N1} (Å)	1.3743	1.3987	1.3972	1.3896	1.3854	1.3226	1.3721	1.3963
R_{C2H} (Å)	1.0773	1.0781	1.0767	1.0761	1.0758	1.0800	1.0760	1.0773
R_{N3H} (Å)	1.0047	1.0161	1.0124	1.0102	1.0089	1.0132	1.0051	1.0168
R_{C4H} (Å)	1.0748	1.0780	1.0757	1.0749	1.0747	1.0793	1.0744	1.0770
R_{C5H} (Å)	1.0766	1.0763	1.0753	1.0749	1.0749	1.0798	1.0757	1.0763
R_{N1Zn} (Å)		1.8840	1.8769	1.9682	2.0400			1.8529
θ_{C2N1C5} (°)	105.5	108.2	107.2	106.7	106.4	106.1	105.0	108.1
θ_{N3C2N1} (°)	111.5	107.7	108.8	109.6	110.0	111.6	111.6	107.5
θ_{C4N3C2} (°)	107.3	110.3	109.8	109.1	108.7	107.4	107.6	110.8
θ_{C5C4N3} (°)	105.1	106.8	106.2	105.9	105.7	104.9	104.9	106.5
θ_{N1C5C4} (°)	110.6	106.8	108.0	108.8	109.1	109.9	110.9	107.2
D_0 (kJ/mol)		766.0	1296.8	1564.3	1751.3			710.9
D_0 [a] (kJ/mol)		766.0	648.4	521.4	437.8			710.9
σ [a] (cm^{-1})		304	318	271	239			347
q_{Zn} (e)		1.61	1.50	1.39	1.24			1.84
q_{Im} (e)	0	0.39	0.25	0.20	0.19	1	0	0.16

frequencies verified the nature of the planar and bent structures as transition state and minimum, respectively. For example, the imaginary frequencies of the planar transition states are i1125 (i555) cm^{-1} using the (aug-)cc-pVTZ basis set. Nonetheless, the low barriers to planarity indicate that the zero-point vibrational level is probably above the barrier leading to a quasi-planar complex.

To test the effects of electron correlation on the Zn^{2+}–Im interaction, calculations were performed at the MP2 level using basis sets up to cc-pVTZ. The MP2/cc-pVTZ calculations yield a planar minimum structure, with $R_{ZnN} = 1.853$ Å and $D_0 = 711$ kJ/mol, which are to be compared to the corresponding B3LYP/cc-pVTZ values of $R_{ZnN} = 1.884$ Å and $D_0 = 766$ kJ/mol, respectively. Thus, the MP2 interaction energy is roughly 55 kJ/mol (7%) weaker than the B3LYP energy, in good agreement with previous observations [10,15]. The NBO analysis at the MP2 level yields a smaller charge transfer from Zn^{2+} to Im than the B3LYP level (0.17 vs. 0.39 e), which may partly account for the difference in the calculated interaction energies. Although strong σ and weak π donation was previously reported also on the basis of MP2 calculations [15], the B3LYP level might overestimate to some extent the charge transfer arising from both donation mechanisms, leading to a stronger interaction and the slight deviation from planarity. Further theoretical and experimental investigations, which are beyond the scope of the present work, are required to decide which of the two theoretical approaches provides a slightly more reliable description of the Zn^{2+}–Im interaction.

The investigated $[ZnIm_2]^{2+}$ minimum has C_2 symmetry with the two equivalent Im ligands rotated by 90° around the linear N–Zn–N bond (Fig. 1). The planar structure with C_{2v} symmetry is a transition state for internal rotation with a barrier of 3.1 kJ/mol. Interestingly, although the binding energy per Im ligand in $[ZnIm_2]^{2+}$ is substantially weaker than in $[ZnIm]^{2+}$ (by ∼15%), $D_0^a =$ 648 kJ/mol vs. 766 kJ/mol, the Zn–Im bond is slightly shorter ($R_{ZnN} = 1.877$ Å vs. 1.884 Å). The latter observation is in line with the slightly higher value for the averaged Zn–N stretching frequency of $\sigma_{ZnN}^a = 318\ cm^{-1}$ derived from the symmetric and antisymmetric normal modes, $\sigma_{ZnN}(s) = 231\ cm^{-1}$ and $\sigma_{ZnN}(a) = 406\ cm^{-1}$. A similar bond contraction upon attachment of the second ligand has previously been predicted for the related $[Zn(H_2O)_{1,2}]^{2+}$ and isoelectronic $[Cu(H_2O)_{1,2}]^+$ and $[Cu(NH_3)_{1,2}]^+$ complexes [18,27]. On the other hand, B3LYP/6-31G* calculations for $[CuIm_{1,2}]^+$ predict a Cu–N bond elongation upon increasing n from 1 to 2 [25]. In comparison to $[ZnIm]^{2+}$, the total metal-to-ligand charge transfer in $[ZnIm_2]^{2+}$ is larger (0.50 e vs. 0.39 e), although the transfer to individual Im ligands is smaller ($q_{Im} = 0.25$ e vs. 0.39 e). The linear N–Zn–N configuration is consistent with the well-known preference of Zn^{2+} to form a linear coordination in $[ZnL_2]^{2+}$ ions, which arises from its $d^{10}s^0$ electronic configuration. Mixing of the 4s and $3d_{z^2}$ orbitals leads to a $d^{10-x}s^x$ configuration. The resulting hybrid orbitals feature reduced electron density along the z-axis and generate two favorable binding sites for electron donating ligands in a linear L–Zn^{2+}–L configuration [18,27,60,92]. This effect is more pronounced than the weak stabilizing effect of π donation observed in the nonplanar $[ZnIm]^{2+}$ dimer, so that the Zn^{2+} ion in $[ZnIm_2]^{2+}$ interacts with the N atoms of the two Im ligands in the aromatic plane.

The considered $[ZnIm_3]^{2+}$ minimum shown in Fig. 1 has three nearly identical Im ligands attached to the central Zn cation. The three basic N atoms of the three Im ligands form an essentially regular triangle with Zn in its center, leading to a trigonal planar configuration with $R_{NN} \sim 3.409$ Å. The average of the three nearly identical Zn–N distances amounts to $R_{ZnN}^a = 1.968\,Å$ and is substantially longer than for the considered $n = 1$ and 2 complexes. The orientation of the planar aromatic rings is such that they are rotated out of the plane of the planar trigonal ZnN_3 unit in order to avoid steric hindrance arising from ligand–ligand repulsion [18]. Although the total binding energy of $[ZnIm_3]^{2+}$ is still much larger than for $[ZnIm_2]^{2+}$, the average value decreases again by ∼20%, $D_0^a = 521$ kJ/mol vs. 648 kJ/mol. This observation is in line with an increased total metal-to-ligand charge transfer (0.61 e), corresponding to $q_{Im} = 0.20$ e per Im ligand. The reduced Zn–Im interaction is also reflected in a lower average value for $\sigma_{ZnN}^a =$ 271 cm^{-1}.

The $[ZnIm_4]^{2+}$ minimum shown in Fig. 1 features four quasi equivalent Im ligands attached in a tetrahedral configuration to the central Zn^{2+} cation with N–N distances of $R_{NN} \sim 3.356$ Å. The Zn–N separation of $R_{ZnN}^a = 2.040\,Å$ is again longer than for the $n \leq 3$ complexes and the orientation of the planar aromatic rings is such that they avoid steric hindrance. This trend is accompanied by a further drop in the average binding energy by ∼16% from $D_0^a = 521$ to 438 kJ/mol, which is also reflected in a lower average value for $\sigma_{ZnN}^a = 239\ cm^{-1}$. The IR active component of σ_{ZnN} with t symmetry at 255 cm^{-1} (Fig. 9) compares favorably with measurements from the condensed phase, e.g., $\sigma_{ZnN} = 271\ cm^{-1}$ for $[ZnIm_4]^{2+}(ClO_4^-)_2$ salts [28]. In the tetrahedral $[ZnIm_4]^{2+}$ minimum, the remaining positive charge on the Zn cation is 1.24 e, corresponding to metal-to-ligand charge transfer of $q_{Im} = 0.19$ e

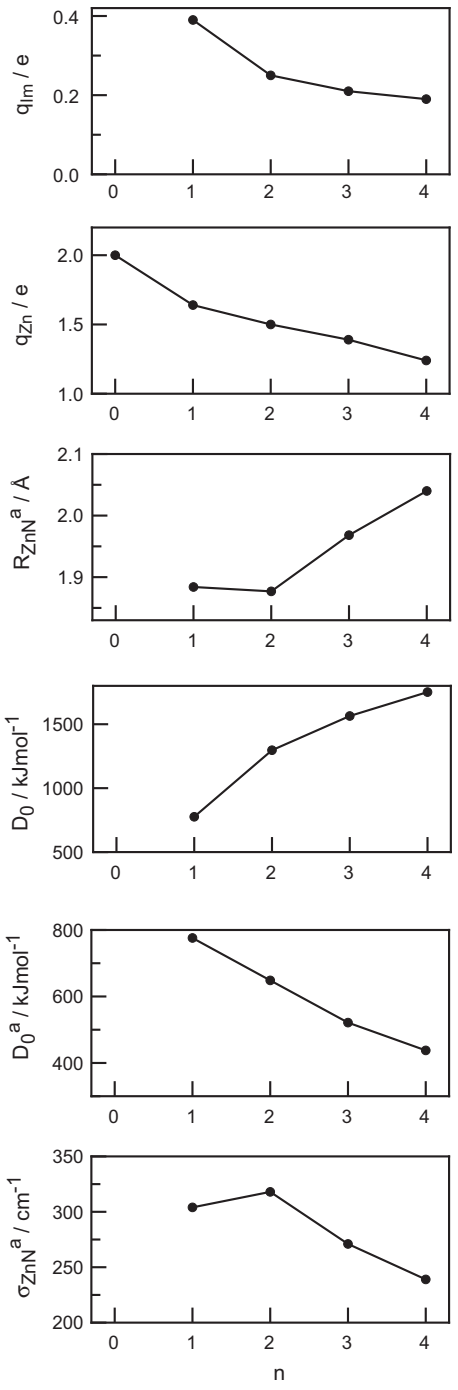

Fig. 7. Selected properties of the Zn–Im metal–ligand bonds in $[ZnIm_n]^{2+}$ complexes (Fig. 1 and Table 2) as a function of the number of ligands in the first coordination shell (n) calculated at the B3LYP/cc-pVTZ level, including the NBO charge on each Im ligand (q_{Im}), the remaining NBO charge on Zn (q_{Zn}), the Zn–N bond distance (R_{ZnN}), the total dissociation energy (D_0), the dissociation energy per Im ligand (D_0^a), and the averaged Zn–N metal–ligand stretch frequency (σ_{ZnN}^a).

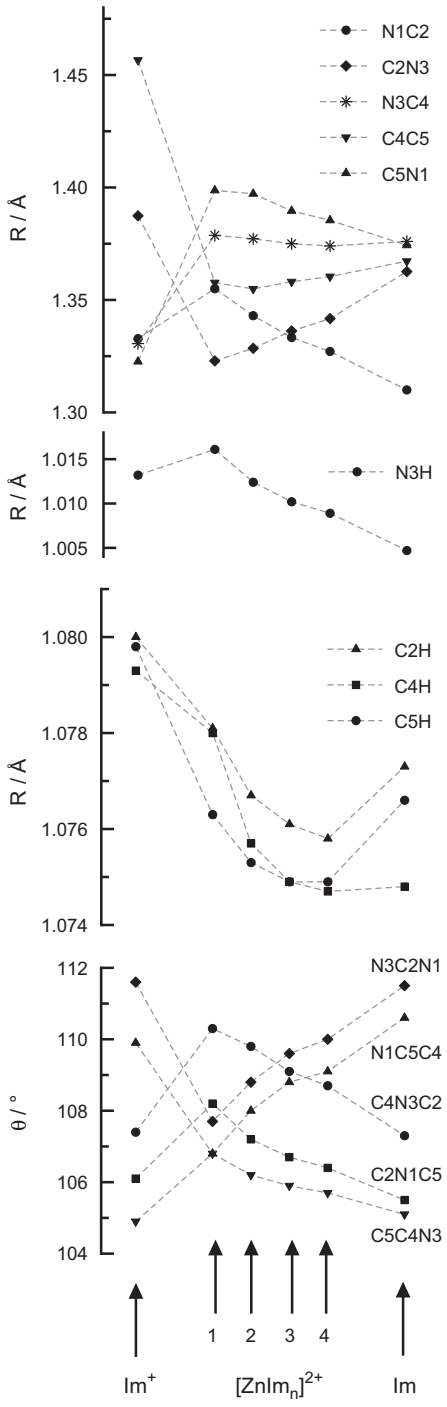

Fig. 8. Selected intramolecular structural parameters of the Im ligands in $[ZnIm_n]^{2+}$ complexes as a function of the number of ligands in the first coordination shell (n) calculated at the B3LYP/cc-pVTZ level compared to corresponding parameters of isolated Im and Im^+ in their ground electronic states (Figs. 1 and 6 and Table 2).

per Im ligand. Interestingly, while $[ZnIm_4]^{2+}$ prefers a tetrahedral coordination shell with CN = 4, the related $[ZnL_4]^{2+}$ ions with L = pyridine adopt a geometry with a planar ZnN_4 core (D_{2d}) and CN = 4 [93]. Efforts to locate a similar structure for $[ZnIm_4]^{2+}$ failed as the tetrahedral configuration is energetically much more stable (by at least 100 kJ/mol).

Fig. 7 summarizes the evolution of salient parameters of the Zn^{2+}–Im interaction in $[ZnIm_n]^{2+}$ as a function of the number of ligands (Table 2). As is typical for interior ion solvation [41,45,94], the average ligand binding energy decreases with n due to noncooperative effects arising from electronic (covalent), electrostatic, and inductive interactions, charge delocalization, and steric hindrance (ligand–ligand repulsion). In the case of $[ZnIm_n]^{2+}$, D_0^a decreases roughly linearly with n in the size range $n \leq 4$ with a slope of about 100 kJ/mol per additional ligand (D_0^a = 766, 648, 521, 438 kJ/mol for n = 1–4). The incremental interaction energies, defined as $D_0(n)$–$D_0(n-1)$, decrease even more dramatically in the size range considered (766, 531, 267, 187 kJ/mol for n = 1–4). Both trends are in line with increasing metal–ligand

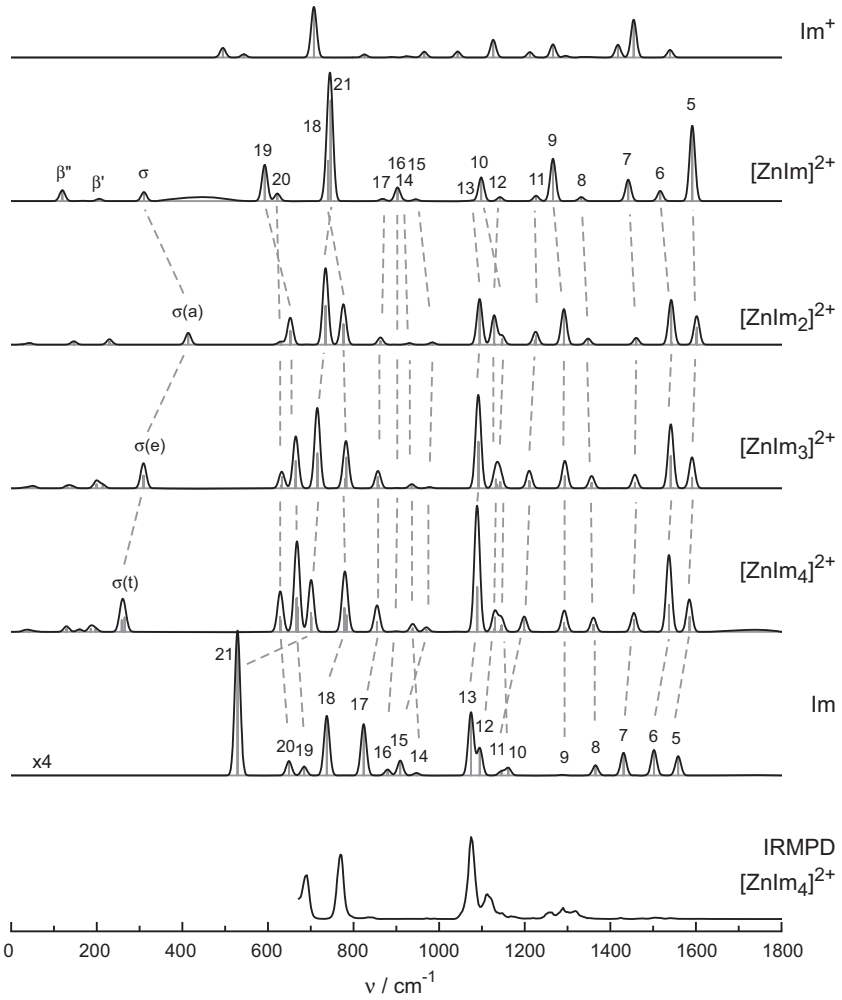

Fig. 9. Linear stick IR absorption spectra of Im, Im^+, and $[ZnIm_n]^{2+}$ with $n = 1–4$ (Fig. 1) calculated at the B3LYP/cc-pVTZ level are compared to the measured IRMPD spectrum of $[ZnIm_4]^{2+}$. The calculated spectra are convoluted with a Gaussian profile with FWHM = 15 cm^{-1}. Corresponding transitions of the imidazole fundamental modes (ν_{5-21}) as well as the Zn–N metal–ligand stretching modes (σ) are connected by dotted lines. The line positions and IR intensities for $[ZnIm_4]^{2+}$ and Im are listed in Table 1. Except for the Im spectrum, which is vertically expanded by a factor of 4, all calculated spectra are drawn to the same scale.

bond lengths and the decreasing effects of charge delocalization on each imidazole ligand (q_{Im} = 0.39, 0.25, 0.20, 0.19 e for $n = 1–4$). These trends established here for $[ZnIm_n]^{2+}$ are qualitatively similar to those predicted previously for the related $[Zn(H_2O)_n]^{2+}$ complexes [18]. At this stage, we note for completeness that there are a variety of $[ZnIm_n]^{2+}$ isomers for the size range $n \geq 3$, which are derived from those shown in Fig. 1 by rotation of one or more Im ligands by ~180° around the Zn–N axis [10]. We calculated some of these isomers for each cluster size and found that they have essentially the same binding energy and very similar Zn–N bond parameters and IR spectral properties. For example, the energy difference of the two investigated rotamers of $[ZnIm_3]^{2+}$ is only 0.1 kJ/mol. Moreover, the B3LYP/cc-pVTZ interaction energies of $[ZnIm_n]^{2+}$ are very similar to those obtained earlier at the B3LYP/6-311++G(d,p) level for $n = 1–3$ (761, 536, and 272 kJ/mol) [10].

After discussing the metal–ligand bond parameters, we turn to the effects of Zn^{2+} complexation on the geometry of the imidazole rings (Figs. 6 and 8 and Table 2). The geometry calculated for Im is in satisfactory agreement with higher level calculations (up to CCSD(T)) and experimental data derived from neutron and X-ray diffraction as well as microwave spectroscopy [74,95]. In particular, the B3LYP/cc-pVTZ data in Table 2 deviate by less than 0.6° and 12 mÅ from the structural parameters obtained from microwave spectroscopy [95]. In general, the impact of Zn^{2+} on the ligand geometry predicted at the MP2 level is similar to that derived at the B3LYP level (Table 2). As a result of the considerable electron donation from the N lone pair to Zn^{2+}, the adjacent N1–C2 and N1–C5 bonds exhibit substantial elongations of ΔR = +45 and +24 mÅ, respectively. This in turn leads to a contraction of the neighboring C2–N3 and C5–C4 bonds of $\Delta R = -40$ and -10 mÅ, respectively, whereas the N3–C4 bond length is nearly unchanged (ΔR = +3 mÅ). In addition to the bond lengths, the ring bond angles are heavily affected. The C2–N1–C5 angle opens up by 2.7°, whereas the adjacent N1–C2–N3 and N1–C5–C4 angles decrease both by 3.8°. Interestingly, while the C–H bond lengths are only little affected by Zn^{2+} complexation ($\Delta R \leq 3$ mÅ), the acidic N–H bond is significantly elongated by 11 mÅ. The latter result indicates the ability of Zn^{2+} to destabilize the N–H bond of Im, which serves in many biocatalytic processes as the proton source for H^+ shuttling [3,24]. For comparison, Figs. 6 and 8 provide also the geometrical parameters of the Im^+ cation in its $^2A''$ ground electronic state, which is obtained from neutral Im by removal of one electron from the bonding 3a″ π orbital (HOMO) delocalized over the aromatic ring [75,77–79]. This comparison reveals that complete single ionization of Im from its HOMO (π) has structurally more pronounced but opposite effects than partial ionization upon Zn^{2+}

attachment via ligand-to-metal electron donation. This result is consistent with the view that charge transfer in $[ZnIm]^{2+}$ is dominated by σ donation to the nonbonding HOMO-1 σ orbital of N rather than π donation to the aromatic ring. Hence, the effects of N-protonation of Im on its structure are qualitatively similar to that of Zn^{2+} complexation [76,80,96].

The evolution of the intramolecular structural parameters of $[ZnIm_n]^{2+}$ is detailed in Table 2 and visualized in Fig. 8. As expected, the largest effect upon Zn^{2+} complexation on the Im ligand geometry is observed for the $[ZnIm]^{2+}$ dimer ($n = 1$). As the charge transfer per individual ligand decreases with n, these changes are less pronounced for $n > 1$ and the structural parameters move more or less monotonically toward those of the isolated Im ligand (with the exception of the C–H bond lengths, which are nearly unaffected anyway). Inspection of Fig. 8 and Table 2 reveals again that the trend in the structural parameters of Im and $[ZnIm_n]^{2+}$ are not linked to the geometric parameters of Im^+, as expected for σ rather than π donation.

The effects of Zn^{2+} complexation on the structural parameters of Im directly translate into shifts in the corresponding vibrational frequencies (Fig. 9). The 21 normal modes of imidazole can be classified in 15 higher-frequency in-plane modes of a′ symmetry (ν_{1-15}) and 6 out-of-plane modes of a″ symmetry (ν_{16-21}), and their fundamental frequencies occur in the 500–3500 cm^{-1} range (Fig. 9 and Table 1) [72–74,97]. The current IRMPD spectrum covers the range of ν_{5-19}, i.e., nearly all ring modes (Fig. 9), whereas the N–H (ν_1) and C–H (ν_{2-4}) stretch fundamentals occur in the 3100–3500 cm^{-1} range not investigated here. The scaled frequencies derived for Im at the B3LYP/cc-pVTZ level agree well with those measured in the gas phase (Table 1) [72]. The small maximum and averaged absolute differences of 20 and 8 cm^{-1}, respectively, confirm that the chosen theoretical level is appropriate to reliably describe the imidazole force field and its vibrational frequencies. The averaged relative deviation of 2 cm^{-1} justifies the choice of the dual scaling factors of 0.98 and 0.96 used for the B3LYP/cc-pVTZ level.

Fig. 9 illustrates the evolution of the IR spectra calculated for $[ZnIm_n]^{2+}$ with $n = 1$–4 along with direct comparison to the spectra calculated for isolated Im and Im^+ in their ground electronic states. Significantly, there are substantial differences in these IR spectra with respect to both the frequencies and IR intensities of various normal modes, confirming that IR spectroscopy is a powerful probe for investigating the effects of ionization and Zn^{2+} complexation on the structural properties of the imidazole chromophore. In $[ZnIm_n]^{2+}$ complexes with more than one Im ligand ($n > 1$), each of the Im monomer modes ν_i gives rise to n intramolecular normal modes in the complex. However, as the coupling between the individual Im ligands is weak, the splitting is generally small (typically <5 cm^{-1}) and below the spectral resolution achieved in the current experiment (see Table S1 in Supporting information for $n = 4$). Hence, we are not considering the splitting of intramolecular modes ν_i further. Instead, Table 1 reports the average frequency and the sum of the IR intensities. This strategy is, however, not applicable to the metal–ligand modes such as σ_{ZnN}, which exhibit much larger couplings and splittings.

According to the geometrical parameters plotted in Fig. 8, the strongest impact of Zn^{2+} complexation on the geometry of the aromatic ligands occurs for the $[ZnIm]^{2+}$ dimer ($n = 1$), because of the highest interaction energy and the largest metal-to-ligand charge transfer. With increasing size of the $[ZnIm_n]^{2+}$ complex, the geometrical parameters develop back toward those of isolated neutral Im. This trend is directly reflected in the IR spectra of $[ZnIm_n]^{2+}$ shown in Fig. 9 and will be discussed in more detail in Section 3.3 for $[ZnIm_4]^{2+}$ concerning modes occurring in the investigated fingerprint range. As already concluded from the evolution of the structural parameters in Fig. 8, the comparison of the IR spectra of $[ZnIm_n]^{2+}$ with that of Im^+ in Fig. 9 clearly confirms that σ donation from the Im ligands to Zn^{2+} dominates the charge transfer in the $[ZnIm_n]^{2+}$ complexes, whereas ionization of Im occurs from the HOMO π orbital to generate Im^+ in the ground electronic state.

The Zn^{2+}–Im metal–ligand modes of $[ZnIm_n]^{2+}$ occur in the spectral range below 400 cm^{-1}, which could not be investigated with the current setup. For example, the metal–ligand stretch, in-plane bend, and out-of-plane bend of Zn^{2+}–Im are calculated as $\sigma = 304$, $\beta' = 202$, and $\beta'' = 117$ cm^{-1}, respectively. In particular, the stretch modes σ_{ZnN} of $[ZnIm_n]^{2+}$ provide a useful probe of the Zn^{2+}–Im interaction strength and the symmetry of the complex. In the $[ZnIm_2]^{2+}$ trimer with C_2 symmetry, σ_{ZnN} splits into a symmetric and antisymmetric component at $\sigma(s) = 231$ and $\sigma(a) = 405$ cm^{-1}, of which only the latter one exhibits significant IR activity (29 km/mol). The $[ZnIm_3]^{2+}$ tetramer with roughly threefold symmetry features one doubly degenerate and one nondegenerate σ_{ZnN} normal mode at $\sigma(e) = 303$ and $\sigma(a) = 208$ cm^{-1}, of which only the former is IR active (61 km/mol). Similarly $[ZnIm_4]^{2+}$ with tetrahedral symmetry has a threefold degenerate and one totally symmetric σ_{ZnN} normal mode at $\sigma(t) = 255$ and $\sigma(a) = 198$ cm^{-1}, of which only the mode with t symmetry is IR allowed (91 km/mol). As is evident from Fig. 7, the averaged frequency of the Zn–N stretch modes (σ^a_{ZnN}) decreases with increasing n due to the reduction in the Zn–N bond strength.

Interestingly, while the C–H bond lengths and corresponding stretch frequencies of Im are nearly unaffected by complexation with Zn^{2+}, the acidic N–H bonds in $[ZnIm_n]^{2+}$ exhibit substantial bond length changes and frequency shifts as n changes. The large destabilization of the N–H bond in the $[ZnIm]^{2+}$ dimer ($\Delta R_{NH} = +11.4$ mÅ) translates into a frequency redshift of $\Delta\nu_1 = -116$ cm^{-1} and an enhancement in its IR intensity by a factor of 6.4 from 52 to 333 km/mol. As the number of Im ligands increase from $n = 2$–4, the N–H bond elongation becomes less pronounced ($\Delta R_{NH} = +7.7$, +5.5, 4.2 mÅ), and the total redshift decreases accordingly ($\Delta\nu_1 = -73$, −50, −36 cm^{-1}). Thus, the N–H bond destabilization is maximal for $n = 1$ and monotonically reduced when the first coordination shell is filled. Comparison of the experimental ν_1 frequency of Im (3504 cm^{-1} [72]), Im^+ (3433 cm^{-1} [75]) and ImH^+ (3470 cm^{-1} [80]) with the predicted value of 3474 cm^{-1} for $[ZnIm_4]^{2+}$ suggests that the N–H bond strengths in ImH^+ and $[ZnIm_4]^{2+}$ are rather similar, i.e., protonation of Im has a similar destabilizing effect on the N–H bond as inserting Im in a tetrahedral $[ZnIm_4]^{2+}$ environment often encountered in active centers of Zn enzymes.

3.3. Assignment of IRMPD spectrum

Fig. 10 compares the measured IRMPD spectrum of $[ZnIm_4]^{2+}$ with the linear IR absorption spectrum calculated for the isomer shown in Fig. 1. The corresponding peak positions and assignments are listed in Table 1. There is good correspondence between the two IR spectra with respect to the frequencies of the transitions, confirming the given vibrational assignments. All transitions with predicted IR intensities larger than a critical threshold intensity of $I_c \sim 30$ km/mol are clearly identified in the measured IRMPD spectrum. Such a threshold is typical for IRMPD spectra, and its magnitude depends on several factors, including the size and binding energy of the ion [54,64,65]. The bands O–R occur in the spectral range of the P-branch of the H_2O bend vibration (ν_2). Thus, it is possible that their intensity may significantly be reduced due to atmospheric water absorptions in the IR-FEL laser beam path. The FEL power displayed in Fig. 5 was measured as single points directly at the FEL exit and not close to the ion trap mass spectrometer. Clearly, the overall appearance of the IRMPD spectrum of $[ZnIm_4]^{2+}$ differs largely from that of Im^+ (Fig. 9), providing experimental confirmation for the domination of σ donation in the charge transfer mechanism in $[ZnIm_n]^{2+}$.

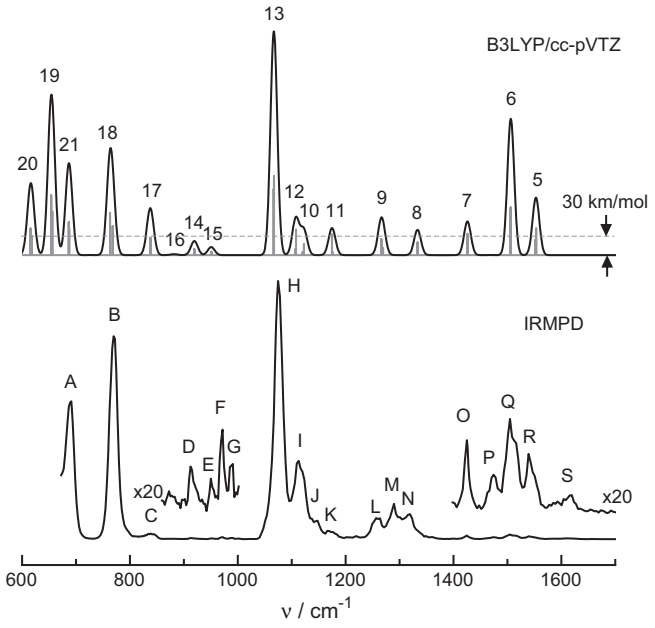

Fig. 10. Comparison of the IRMPD spectrum of $[ZnIm_4]^{2+}$ with the linear IR absorption spectrum calculated for the isomer shown in Fig. 1 at the B3LYP/cc-pVTZ level. The positions and assignments of the transitions are listed in Table 1. The intensity of the bands O–R may significantly be reduced due to atmospheric water absorptions in the IR-FEL laser beam path (see text).

The intense band A at 690 cm^{-1} is assigned to the out-of-plane N–H bending mode ν_{21} of $[ZnIm_4]^{2+}$, which exhibits a substantial blueshift of ~+150 cm^{-1} from the transition in the isolated Im molecule, in line with the theoretical prediction of +169 cm^{-1}. Thus, while the acidic N–H bond becomes weaker and longer in the $[ZnIm_4]^{2+}$ complex, the force constant for out-of-plane motion increases considerably. This is not an effect of steric hindrance arising from ligand–ligand repulsion, because a large blueshift is already predicted for the $[ZnIm]^{2+}$ dimer with $n = 1$, $\Delta\nu_{21}$ = +213 cm^{-1}. The strong transition B at 770 cm^{-1} is attributed to the symmetric out-of-plane C–H bend ν_{18} of $[ZnIm_4]^{2+}$ involving mainly C4–H and C5–H. Similar to the out-of-plane N–H bend ν_{21}, this C–H bend displays a blueshift with respect to Im of +35 cm^{-1}, consistent with the predicted value of $\Delta\nu_{18}$ = +42 cm^{-1}. Transition C at 840 cm^{-1}, assigned to the out-of-plane C2–H bend ν_{17} of $[ZnIm_4]^{2+}$, shows a similar blueshift of +30 cm^{-1}, close to the predicted shift of $\Delta\nu_{17}$ = +31 cm^{-1}. The transitions D–G in the IRMPD spectrum are very weak and their assignment is somewhat tentative. By comparison with the calculations, D and E are attributed to the ring modes ν_{14} and ν_{15}, which are indeed predicted to have only low IR activity (I < 20 km/mol). While ν_{14} exhibits almost no shift as compared to bare Im, ν_{15} has a large blueshift ($\Delta\nu_{14}$ = −3 cm^{-1}, $\Delta\nu_{15}$ = +58 cm^{-1}), in good agreement with the prediction ($\Delta\nu_{14}$ = −9 cm^{-1}, $\Delta\nu_{15}$ = +60 cm^{-1}). Band H at 1081 cm^{-1} dominates the IR spectrum of $[ZnIm_4]^{2+}$ in the investigated range. It is readily assigned to the in-plane C–H bending mode ν_{13}, and its measured blueshift of +25 cm^{-1} from the value for isolated Im compares favorably with the predicted value of +15 cm^{-1}. Band I centered at 1112 cm^{-1} and its shoulder near 1120 cm^{-1} are attributed to the overlapping modes ν_{12} and ν_{10} of $[ZnIm_4]^{2+}$. They also correspond to in-plane C–H bend modes. Moreover, ν_{10} exhibits significant coupling with the N–H bend. Thus, similar to ν_{13}, the bare C–H bend ν_{12} is blueshifted compared to isolated Im by +41 cm^{-1}, in agreement with the prediction (+35 cm^{-1}), while ν_{10} is nearly unaffected. Band K at 1169 cm^{-1} is assigned to ν_{11} of $[ZnIm_4]^{2+}$, which is a highly coupled mode involving in-plane C–H and N–H bending as well as symmetric stretching of the N1–C5 and N3–C4 bonds. The net effect is a measured blueshift of $\Delta\nu_{11}$ = +39 cm^{-1}, which is compatible with the theoretical shift (+52 cm^{-1}). Band L is attributed to ν_9 of $[ZnIm_4]^{2+}$, a coupled mode composed of in-phase C–H and N–H bending as well as asymmetric stretching of the N1–C2 and N1–C5 bonds. The small measured shift of +6 cm^{-1} coincides with the calculated shift. Similar conclusions apply to band N at 1318 cm^{-1} attributed to ν_8 of $[ZnIm_4]^{2+}$. This normal mode is similar to ν_9, although with different phases of certain atomic displacements, and thus also exhibits only minor measured and predicted shifts of $\Delta\nu_8$ = −7 and −4 cm^{-1}, respectively. Bands O, Q, and R observed at 1425, 1509, and 1539 cm^{-1} correspond to the various remaining C–C and C–N stretching modes ν_{5-7}, which all exhibit measured blueshifts of 20–30 cm^{-1}, in accordance with the predicted shifts of 25–35 cm^{-1}.

Three bands with significant IR intensity appear in the IRMPD spectrum of $[ZnIm_4]^{2+}$, which cannot readily be attributed to fundamental modes, namely the bands M, P, and S occurring at 1289, 1474, and 1614 cm^{-1}, respectively. These transitions are probably due to overtone or combination bands. For example, band P at 1474 cm^{-1} is close to the position predicted for the combination of two intense fundamentals $\nu_{18} + \nu_{21}$ (770 + 690 = 1460 cm^{-1}), while band M at 1289 cm^{-1} is near $2\nu_{19}$ expected at around 2×655 = 1310 cm^{-1}. Similarly, band S at 1614 cm^{-1} might be due to $\nu_{17} + \nu_{18}$ estimated as 770 + 840 = 1610 cm^{-1} from their fundamental frequencies.

The agreement between experimental and the scaled calculated vibrational frequencies for the 14 assigned fundamental frequencies in the IR spectrum of $[ZnIm_4]^{2+}$ is better than 16 cm^{-1}, with an average deviation of 6 cm^{-1}. This degree of agreement is comparable with the experimental spectral resolution of ~10 cm^{-1} and thus provides significant confidence for the vibrational assignment. Moreover, there seems to be no noticeable systematic shift of the experimental band positions to lower frequencies induced by the multiple photonic nature of the IRMPD process. This observation may be taken as experimental evidence that only comparably few photons are required to drive photodissociation of $[ZnIm_4]^{2+}$ into the charge-separated ImH^+ and $[Zn(Im–H)Im_2]^+$ fragment ions, which involves a Coulomb barrier. Calculations at the B3LYP/cc-pVTZ level yield 47 kJ/mol for the dissociation energy of $[ZnIm_4]^{2+}$ into separated ImH^+ and $[Zn(Im–H)Im_2]^+$, which is much lower than the dissociation of a neutral ligand (~200 kJ/mol). In the IRMPD spectra of strongly bound aromatic ions, some of the high-frequency ring modes usually show significant redshifts compared to scaled linear IR absorption spectra [59,60,63,65]. Significantly, IR spectra calculated for $[ZnIm_n]^{2+}$ isomers with Im ligands in the second solvation shell have a very different IR spectrum in the fingerprint range and can thus be excluded as carrier of the measured IRMPD spectrum (see Fig. S2 in Supporting information).

Finally, the frequencies of isolated $[ZnIm_4]^{2+}$ derived from the IRMPD spectrum are compared in Table 1 to the corresponding frequencies measured in $[ZnIm_4](ClO_4)_2$ salts. Although for most modes reasonable agreement is observed, deviations can reach up to 40 cm^{-1} for the modes in the fingerprint range. The most severe perturbations by the crystal environments are noted for the N–H stretch and out-of-plane N–H bend modes, which exhibit shifts of $\Delta\nu_1 \sim -100$ cm^{-1} and $\Delta\nu_{21}$ = +40 cm^{-1}, probably due to the effects of H-bonding of the NH donor group in the crystal environment.

4. Concluding remarks

The IR spectrum of ESI-generated $[ZnIm_4]^{2+}$ complexes derived by IRMPD spectroscopy in the fingerprint range has been analyzed by comparison with density functional calculations. Significantly, the IRMPD spectrum provides the first experimental data for the

biophysically relevant Zn^{2+}–Im interaction in the gas phase, free from interference with the effects of counter ions and solvent. The systematic analysis of quantum chemical calculations for $[ZnIm_n]^{2+}$ with $n = 1–4$ provides detailed insight into the evolution of the Zn^{2+}–Im interaction as the coordination shell is filled. As a general trend, the interaction is strongest for $n = 1$ and decreases monotonically and substantially with increasing n, because the metal-to-ligand charge transfer per ligand becomes less pronounced. This evolution is visible in the properties of the metal–ligand bonds as well as the corresponding impact on the intramolecular parameters of the Im ligands and the resulting IR spectra. Significantly, the comparison of the properties of $[ZnIm_n]^{2+}$ with those of Im and Im^+ confirms that charge transfer from the metal ion to the ligand is dominated by σ donation. The mass spectrometric and the IR spectroscopic results suggest that the preferred coordination number of $[ZnIm_n]^{2+}$ complexes in solution is CN = 4 with a tetrahedral configuration, under the realistic assumption that the ESI-generated ions do not change coordination upon the electrospray process.

Several directions for further studies emerge from the current work. First, the IR spectroscopic results for $[ZnIm_4]^{2+}$ provides the basis for the analysis of the measured IR spectra of $[ZnOHIm_n]^+$ [14], which will be presented elsewhere. The latter complexes directly mimic intermediates in the active centers of Zn enzymes responsible for the protolysis of H_2O into OH^- and H^+. Second, IR spectroscopic investigations in the N–H stretch range using table-top IR lasers will directly probe the effects of Zn^{2+} on the destabilization of the N–H bond in $[ZnImL_3]^{2+}$ or $[ZnHisL_3]^{2+}$ units, responsible for proton shuttling in active centers of Zn enzymes. The present work on $[ZnIm_4]^{2+}$ demonstrates that the fruitful combination of spectroscopy, mass spectrometry, and quantum chemical characterization of metal–organic complexes isolated in the gas phase are a promising route to better understand biochemical processes in active centers of enzymes at the molecular level.

Acknowledgments

This study was supported by *Deutsche Forschungsgemeinschaft* (DO 729/6) and the European Community (project IC 013-06 entitled *IRMPD spectroscopy of metallo-(bio)organic compounds of catalytic interest*). We also appreciate the support by the CLIO teams (J.M. Ortega and P. Maitre).

Appendix A. Supplementary data

Supplementary data associated with this article can be found, in the online version, at doi:10.1016/j.ijms.2011.08.019.

References

[1] K. Nakamoto, Infrared and Raman Spectra of Inorganic and Coordination Compounds, Wiley, New York, 1997.
[2] L. Stryer, Biochemistry, Freeman, New York, 1996.
[3] T. Dudev, C. Lim, Principles governing Mg, Ca, and Zn binding and selectivity in proteins, Chem. Rev. 103 (2003) 773–787.
[4] G. Parkin, Synthetic analogues relevant to the structure and function of zinc enzymes, Chem. Rev. 104 (2004) 699–767.
[5] J.E. Coleman, Zinc enzymes, Curr. Opin. Chem. Biol. 2 (1998) 222–234.
[6] W.N. Lipscomb, N. Strater, Recent advances in zinc enzymology, Chem. Rev. 96 (1996) 2375–2433.
[7] J.M. Berg, Y.G. Shi, The galvanization of biology: a growing appreciation for the roles of zinc, Science 271 (1996) 1081–1085.
[8] R.J. Sundberg, R.B. Martin, Interactions of histidine and other imidazole derivatives with transition-metal ions in chemical and biological systems, Chem. Rev. 74 (1974) 471–517.
[9] W. Maret, Y. Li, Coordination dynamics of zinc in proteins, Chem. Rev. 109 (2009) 4682–4707.
[10] M. Peschke, A.T. Blades, P. Kebarle, Metalloion–ligand binding energies and biological function of metalloenzymes such as carbonic anhydrase. A study based on ab initio calculations and experimental ion–ligand equilibria in the gas phase, J. Am. Chem. Soc. 122 (2000) 1492–1505.
[11] M.T. Rodgers, P.B. Armentrout, A thermodynamic "vocabulary" for metal ion interactions in biological systems, Acc. Chem. Res. 37 (2004) 989–998.
[12] D. Schröder, H. Schwarz, S. Schenk, E. Anders, A gas-phase reaction as a functional model for the activation of carbon dioxide by carbonic anhydrase, Angew. Chem. Int. Edit. 42 (2003) 5087–5090.
[13] H. Cox, A.J. Stace, Recent advances in the visible and UV spectroscopy of metal dication complexes, Int. Rev. Phys. Chem. 29 (2010) 555–588.
[14] O. Dopfer, IRMPD spectroscopy of metallo-(bio)organic compounds of catalytic interest. Report for CLIO project IC 013-06 (2007).
[15] D.R. Garmer, N. Gresh, A comprehensive energy component analysis of the interaction of hard and soft dications with biological ligands, J. Am. Chem. Soc. 116 (1994) 3556–3567.
[16] C.W. Bock, A.K. Katz, J.P. Glusker, Hydration of zinc ions – a comparison with magnesium and beryllium ions, J. Am. Chem. Soc. 117 (1995) 3754–3763.
[17] S. Lee, J. Kim, J.K. Park, K.S. Kim, Ab initio study of the structures, energetics, and spectra of aquazinc(II), J. Phys. Chem. 100 (1996) 14329–14338.
[18] M. Hartmann, T. Clark, R. van Eldik, Hydration and water exchange of zinc(II) ions. Application of density functional theory, J. Am. Chem. Soc. 119 (1997) 7843–7850.
[19] M. Peschke, A.T. Blades, P. Kebarle, Binding energies for doubly-charged ions $M^{2+} = Mg^{2+}$, Ca^{2+} and Zn^{2+} with the ligands $L = H_2O$, acetone and N-methylacetamide in complexes MLn^{2+} for $n = 1–7$ from gas phase equilibria determinations and theoretical calculations, J. Am. Chem. Soc. 122 (2000) 10440–10449.
[20] T.E. Cooper, P.B. Armentrout, Experimental and theoretical investigation of the charge-separation energies of hydrated zinc(II): redefinition of the critical size, J. Phys. Chem. A 113 (2009) 13742–13751.
[21] T.E. Cooper, D.R. Carl, P.B. Armentrout, Hydration energies of zinc(II): threshold collision-induced dissociation experiments and theoretical studies, J. Phys. Chem. A 113 (2009) 13727–13741.
[22] T.E. Cooper, J.T. O'Brien, E.R. Williams, P.B. Armentrout, Zn^{2+} has a primary hydration sphere of five: IR action spectroscopy and theoretical studies of hydrated Zn^{2+} complexes in the gas phase, J. Phys. Chem. A 114 (2010) 12646–12655.
[23] J. El Yazal, Y.P. Pang, Comparison of DFT, Moller–Plesset, and coupled cluster calculations of the proton dissociation energies of imidazole and N-methylacetamide in the presence of zinc(II), J. Mol. Struct. Theochem. 545 (2001) 271–274.
[24] J. El Yazal, Y.P. Pang, Ab initio calculations of proton dissociation energies of zinc ligands: hypothesis of imidazolate as zinc ligand in proteins, J. Phys. Chem. B 103 (1999) 8773–8779.
[25] N.S. Rannulu, M.T. Rodgers, Solvation of copper ions by imidazole: structures and sequential binding energies of $Cu^+(imidazole)_x$, $x = 1–4$. Competition between ion solvation and hydrogen bonding, Phys. Chem. Chem. Phys. 7 (2005) 1014–1025.
[26] N.S. Rannulu, R. Amunugama, Z.B. Yang, M.T. Rodgers, Influence of s and d orbital occupation on the binding of metal ions to imidazole, J. Phys. Chem. A 108 (2004) 6385–6396.
[27] C.W. Bauschlicher, S.R. Langhoff, H. Partridge, The binding energies of $Cu^+–(H_2O)_N$ and $Cu^+–(NH_3)_N$ ($N = 1–4$), J. Chem. Phys. 94 (1991) 2068–2072.
[28] J.B. Hodgson, G.C. Percy, D.A. Thornton, The infrared spectra of imidazole complexes of 1st transition series metal(II) nitrates and perchlorates, J. Mol. Struct. 66 (1980) 81–92.
[29] B. Cornilsen, K. Nakamoto, Metal isotope effect on metal–ligand vibrations. 12. Imidazole complexes with Co(II), Ni(II), Cu(II) and Zn(II), J. Inorg. Nucl. Chem. 36 (1974) 2467–2471.
[30] D.M. Goodgame, M. Goodgame, P.J. Hayward, G.W. Rayner-Canham, Low-energy vibrational spectra of some imidazole complexes, Inorg. Chem. 7 (1968) 2447.
[31] M. Andersson, J. Hedin, P. Johansson, J. Nordstrom, M. Nyden, Coordination of imidazoles by Cu(II) and Zn(II) as studied by NMR relaxometry, EPR, far-FTIR vibrational spectroscopy and ab initio calculations: effect of methyl substitution, J. Phys. Chem. A 114 (2010) 13146–13153.
[32] M.A. Duncan, Spectroscopy of metal ion complexes, Annu. Rev. Phys. Chem. 48 (1997) 69.
[33] M.A. Duncan, Frontiers in the spectroscopy of mass selected molecular ions, Int. J. Mass Spectrom. 200 (2000) 545.
[34] M.A. Duncan, IR spectroscopy of metal ion complexes, Int. Rev. Phys. Chem. 22 (2003) 407.
[35] M.A. Duncan, Structures, energetics and spectroscopy of gas phase transition metal ion-benzene complexes, Int. J. Mass Spectrom. 272 (2008) 99–118.
[36] L. MacAleese, P. Maitre, Infrared spectroscopy of organometallic ions in the gas phase: from model to real world complexes, Mass Spectrom. Rev. 26 (2007) 583–605.
[37] J. Lemaire, P. Boissel, M. Heninger, G. Mauclaire, G. Bellec, H. Mestdagh, A. Simon, S. Le Caer, J.M. Ortega, F. Glotin, P. Maitre, Gas phase IR spectroscopy of selectively prepared ions, Phys. Rev. Lett. 89 (2002) 273002.
[38] J. Oomens, D.T. Moore, G. von Helden, G. Meijer, R.C. Dunbar, The site of Cr^+ attachment to gas-phase aniline from infrared spectroscopy, J. Am. Chem. Soc. 126 (2004) 724–725.
[39] T. Baer, R.C. Dunbar, Ion spectroscopy: where did it come from; where is it now; and where is it going? J. Am. Soc. Mass Spectrom. 21 (2010) 681–693.
[40] M. Okumura, L.I. Yeh, J.D. Myers, Y.T. Lee, Infrared spectra of the solvated hydronium ion: vibrational predissociaation spectroscopy of mass-selected $H_3O^+(H_2O)_n(H_2)_m$, J. Phys. Chem. 94 (1990) 3416–3427.

[41] O. Dopfer, Spectroscopic and theoretical studies of CH_3^+–Rg_n clusters (Rg = He, Ne, Ar): from weak intermolecular forces to chemical reaction mechanisms, Int. Rev. Phys. Chem. 22 (2003) 437.
[42] E.J. Bieske, Spectroscopic studies of anion complexes und clusters, Chem. Soc. Rev. 32 (2003) 231.
[43] E.J. Bieske, O. Dopfer, High resolution spectroscopy of cluster ions, Chem. Rev. 100 (2000) 3963.
[44] O. Dopfer, IR spectroscopic strategies for the structural characterization of isolated and microsolvated arenium ions, J. Phys. Org. Chem. 19 (2006) 540–551.
[45] O. Dopfer, IR spectroscopy of microsolvated aromatic cluster ions: ionization-induced switch in aromatic molecule—solvent recognition, Z. Phys. Chem. 219 (2005) 125.
[46] J.M. Lisy, Infrared studies of ionic clusters: the influence of Yuan T. Lee, J. Chem. Phys. 125 (2006) 19.
[47] W.H. Robertson, M.A. Johnson, Molecular aspects of halide anion hydration, Annu. Rev. Phys. Chem. 54 (2003) 173.
[48] J.R. Roscioli, L.R. McCunn, M.A. Johnson, Quantum structure of the intermolecular proton bond, Science 316 (2007) 249–254.
[49] T. Ebata, A. Fujii, N. Mikami, Vibrational spectroscopy of small sized hydrogen bonded clusters and their ions, Int. Rev. Phys. Chem. 17 (1998) 331.
[50] T.R. Rizzo, J.A. Stearns, O.V. Boyarkin, Spectroscopic studies of cold, gas-phase biomolecular ions, Int. Rev. Phys. Chem. 28 (2009) 481–515.
[51] H. Schneider, K.M. Vogelhuber, F. Schinle, J.M. Weber, Aromatic molecules in anion recognition: electrostatics versus H-bonding, J. Am. Chem. Soc. 129 (2007) 13022–13026.
[52] K.R. Asmis, J. Sauer, Mass-selective vibrational spectroscopy of vanadium oxide cluster ions, Mass Spectrom. Rev. 26 (2007) 542–562.
[53] J. Oomens, A.G.G.M. Tielens, B.G. Sartakov, G. von Helden, G. Meijer, Laboratory infrared spectroscopy of cationic polycyclic aromatic hydrocarbon molecules, Astrophys. J. 591 (2003) 968.
[54] J. Oomens, B.G. Sartakov, G. Meijer, G. von Helden, Gas-phase IRMPD spectroscopy of mass-selected molecular ions, Int. J. Mass Spectrom. 254 (2006) 1–19.
[55] N.C. Polfer, J. Oomens, Vibrational spectroscopy of bare and solvated ionic complexes of biological relevance, Mass Spectrom. Rev. 28 (2009) 468–494.
[56] J.R. Eyler, Infrared multiple photon dissociation spectroscopy of ions in penning traps, Mass Spectrom. Rev. 28 (2009) 448–467.
[57] T.D. Fridgen, Infrared consequence spectroscopy of gaseous protonated and metal ion cationized complexes, Mass Spectrom. Rev. 28 (2009) 586–607.
[58] B.M. Reinhard, A. Lagutschenkov, J. Lemaire, P. Maitre, P. Boissel, G. Niedner-Schatteburg, Reductive nitrile coupling in niobium–acetonitrile complexes probed by free electron laser IR multiphoton dissociation spectroscopy, J. Phys. Chem. A 108 (2004) 3350–3355.
[59] A. Lagutschenkov, R.K. Sinha, P. Maitre, O. Dopfer, Structure and infrared spectrum of the Ag^+–phenol ionic complex, J. Phys. Chem. A 114 (2010) 11053–11059.
[60] S. Chakraborty, O. Dopfer, Infrared spectrum of the Ag^+–$(pyridine)_2$ ionic complex: probing the interactions in artificial metal-mediated base pairing, Chem. Phys. Chem. 12 (2011) 1999–2008.
[61] M. Savoca, T. Wende, L. Jiang, J. Langer, G. Meijer, O. Dopfer, K.R. Asmis, Infrared spectra and structures of silver-PAH cation complexes, J. Phys. Chem. Lett. 2 (2011) 2052–2056.
[62] A. Lagutschenkov, A. Springer, U.J. Lorenz, P. Maitre, O. Dopfer, Structure of zirconocene complexes relevant for olefin catalysis: IR fingerprint of the $Zr(C_5H_5)_2(OH)(CH_3CN)^+$ cation in the gas phase, J. Phys. Chem. A 114 (2010) 2073–2079.
[63] H. Knorke, J. Langer, J. Oomens, O. Dopfer, Infrared spectra of isolated protonated polycyclic aromatic hydrocarbon molecules, Astrophys. J. Lett. 706 (2009) L66–L70.
[64] D. Zhao, J. Langer, J. Oomens, O. Dopfer, Infrared spectra of protonated polycyclic aromatic hydrocarbon molecules: azulene, J. Chem. Phys. 131 (2009) 184307.
[65] A. Lagutschenkov, O. Dopfer, Infrared spectrum of a protonated fluorescence dye: acridine orange, J. Mol. Spectrosc. 268 (2011) 66–77.
[66] A. Lagutschenkov, J. Langer, G. Berden, J. Oomens, O. Dopfer, Infrared spectra of protonated neurotransmitters: serotonin, J. Phys. Chem. A 114 (2010) 13268–13276.
[67] A. Lagutschenkov, J. Langer, G. Berden, J. Oomens, O. Dopfer, Infrared spectra of protonated neurotransmitters: dopamine, Phys. Chem. Chem. Phys. 13 (2011) 2815–2823.
[68] A. Lagutschenkov, J. Langer, G. Berden, J. Oomens, O. Dopfer, Infrared spectra of the protonated neurotransmitter histamine: competition between imidazolium and ammonium isomers in the gas phase, Phys. Chem. Chem. Phys. 13 (2011) 15644–15656.
[69] N.C. Polfer, J. Oomens, D.T. Moore, G. von Helden, G. Meijer, R.C. Dunbar, Infrared spectroscopy of phenylalanine Ag(I) and Zn(II) complexes in the gas phase, J. Am. Chem. Soc. 128 (2006) 517–525.
[70] T.E. Cooper, D.R. Carl, J. Oomens, J.D. Steill, P.B. Armentrout, Infrared spectroscopy of divalent zinc and cadmium crown ether systems, J. Phys. Chem. A 115 (2011) 5408–5422.
[71] B. Chiavarino, M.E. Crestoni, S. Fornarini, F. Lanucara, J. Lemaire, P. Maitre, D. Scuderi, Direct probe of NO vibration in the naked ferric heme nitrosyl complex, Chem. Phys. Chem. 9 (2008) 826–828.
[72] S.T. King, Low-temperature matrix isolation study of hydrogen-bonded, high-boiling organic compounds. 1. Sampling device and infrared spectra of pyrazole, imidazole, and dimethyl phosphinic acid, J. Phys. Chem. 74 (1970) 2133.
[73] M. van Bael, J. Smets, K. Schoone, L. Houben, W. McCarthy, L. Adamowicz, M.J. Nowak, G. Maes, Matrix-isolation FTIR studies and theoretical calculations of hydrogen-bonded complexes of imidazole. A comparison between experimental results and different calculation methods, J. Phys. Chem. A 101 (1997) 2397.
[74] A.A. El-Azhary, A coupled-cluster study of the structure and vibrational spectra of pyrazole and imidazole, Spectrochim. Acta A: Mol. Biomol. Spectrosc. 59 (2003) 2009–2025.
[75] H.S. Andrei, N. Solca, O. Dopfer, Interaction of ionic biomolecular building blocks with nonpolar solvents: acidity of the imidazole cation (Im^+) probed by IR spectra of Im^+–L_n complexes (L = Ar, N_2; $n \leq 3$), J. Phys. Chem. A 109 (2005) 3598–3607.
[76] H.K. Gerardi, G.H. Gardenier, U. Viswanathan, S.M. Auerbach, M.A. Johnson, Vibrational predissociation spectroscopy and theory of Ar-tagged, protonated imidazole (Im) $Im_{1-3}H^+$·Ar clusters, Chem. Phys. Lett. 501 (2011) 172–178.
[77] J. Main-Bobo, S. Olesik, W. Gase, T. Baer, A.A. Mommers, J.L. Holmes, The thermochemistry and dissociation dynamics of energy-selected pyrazole and imidazole ions, J. Am. Chem. Soc. 108 (1986) 677.
[78] S. Cradock, R.H. Findlay, M.H. Palmer, Molecular energy levels of azoles – study by photoelectron spectroscopy and ab-initio molecular orbital calculations, Tetrahedron 29 (1973) 2173.
[79] B.G. Ramsey, Substituent effects on imidazole basicity and photoelectron-spectroscopy determined ionization energies, J. Org. Chem. 44 (1979) 2093.
[80] H.S. Andrei, N. Solcà, O. Dopfer, Microhydration of protonated biomolecular building blocks: IR spectra of protonated imidazole–$water_n$ complexes, Chem. Phys. Chem. 7 (2006) 107–110.
[81] L. MacAleese, A. Simon, T.B. McMahon, J.M. Ortega, D. Scuderi, J. Lemaire, P. Maitre, Mid-IR spectroscopy of protonated leucine methyl ester performed with an FTICR or a Paul type ion-trap, Int. J. Mass Spectrom. 249–250 (2006) 14–20.
[82] R. Prazeres, F. Glotin, C. Insa, D.A. Jaroszynski, J.M. Ortega, Two-colour operation of a free electron laser and applications in the mid-infrared, Eur. Phys. J. D 3 (1998) 87.
[83] M.J. Frisch, G.W. Trucks, H.B. Schlegel, G.E. Scuseria, M.A. Robb, J.R. Cheeseman, G. Scalmani, V. Barone, B. Mennucci, G.A. Petersson, H. Nakatsuji, M. Caricato, X. Li, H.P. Hratchian, A.F. Izmaylov, J. Bloino, G. Zheng, J.L. Sonnenberg, M. Hada, M. Ehara, K. Toyota, R. Fukuda, J. Hasegawa, M. Ishida, T. Nakajima, Y. Honda, O. Kitao, H. Nakai, T. Vreven, J.A. Montgomery Jr., J.E. Peralta, F. Ogliaro, M. Bearpark, J.J. Heyd, E. Brothers, K.N. Kudin, V.N. Staroverov, R. Kobayashi, J. Normand, K. Raghavachari, A. Rendell, J.C. Burant, S.S. Iyengar, J. Tomasi, M. Cossi, N. Rega, J.M. Millam, M. Klene, J.E. Knox, J.B. Cross, V. Bakken, C. Adamo, J. Jaramillo, R. Gomperts, R.E. Stratmann, O. Yazyev, A.J. Austin, R. Cammi, C. Pomelli, J.W. Ochterski, R.L. Martin, K. Morokuma, V.G. Zakrzewski, G.A. Voth, P. Salvador, J.J. Dannenberg, S. Dapprich, A.D. Daniels, Ö. Farkas, J.B. Foresman, J.V. Ortiz, J. Cioslowski, D.J. Fox, Gaussian09, Rev. A.1. Gaussian, Inc., Wallingford, CT, 2009.
[84] M.D. Halls, J. Velkovski, H.B. Schlegel, Harmonic frequency scaling factors for Hartree-Fock, S-VWN, B-LYP, B3-LYP, B3-PW91 and MP2 with the Sadlej pVTZ electric property basis set, Theor. Chem. Acc. 105 (2001) 413–421.
[85] D. Moran, A.C. Simmonett, F.E. Leach, W.D. Allen, P.V. Schleyer, H.F. Schaefer, Popular theoretical methods predict benzene and arenes to be nonplanar, J. Am. Chem. Soc. 128 (2006) 9342–9343.
[86] E.P.L. Hunter, S.G. Lias, Evaluated gas phase basicities and proton affinities of molecules: an update, J. Phys. Chem. Ref. Data 27 (1998) 413.
[87] R.A. Jockusch, E.R. Williams:, Binding energies of proton-bound dimers of imidazole and n-acetylalanine methyl ester obtained by blackbody infrared radiative dissociation, J. Phys. Chem. A 102 (1998) 4543–4550.
[88] H.S. Andrei, Infrared photodissociation spectroscopy of ionic hydrocarbons: microsolvation and protonation sites, PhD thesis, University of Würzburg (Germany) (2007).
[89] A.T. Blades, P. Jayaweera, M.G. Ikonomou, P. Kebarle, Ion-molecule clusters involving doubly charged metal-ions (M^{2+}), Int. J. Mass Spectrom. Ion Processes 102 (1990) 251–267.
[90] A.A. Shvartsburg, K.W.M. Siu, Is there a minimum size for aqueous doubly charged metal cations? J. Am. Chem. Soc. 123 (2001) 10071–10075.
[91] B. Chiavarino, M.E. Crestoni, S. Fornarini, O. Dopfer, J. Lemaire, P. Maitre, IR spectroscopic features of gaseous $C_7H_7O^+$ ions: benzylium versus tropylium ion structures, J. Phys. Chem. A 110 (2006) 9352.
[92] L.E. Orgel:, Stereochemistry of metals of the B sub-groups. 1. Ions with filled d-electron shells, J. Chem. Soc. (1958) 4186–4190.
[93] G.H. Wu, C. Norris, H. Stewart, H. Cox, A.J. Stace, State-resolved UV photofragmentation spectrum of the metal dication complex $[Zn(pyridine)_4]^{2+}$, Chem. Commun. (2008) 4153–4155.
[94] R.G. Keesee, A.W. Castleman Jr., Thermochemical data on gas-phase ion-molecule association and clustering reactions, J. Phys. Chem. Ref. Data 15 (1986) 1011–1071.
[95] D. Christen, J.H. Griffiths, J. Sheridan, The microwave-spectrum of imidazole – complete structure and the electron-distribution from nuclear-quadrupole coupling tensors and dipole-moment orientation, Zeitschrift Für Naturforschung Section A 36 (1981) 1378–1385.
[96] A.A. Adesokan, G.M. Chaban, O. Dopfer, R.B. Gerber, Vibrational spectroscopy of protonated imidazole and its complexes with water molecules: ab initio anharmonic calculations and experiments, J. Phys. Chem. A 111 (2007) 7374–7381.
[97] M. Majoube, G. Vergoten, Assignment of normal-modes for imidazole on the basis of 3-21G and 4-21G ab initio force fields, J. Mol. Spectrosc. 266 (1992) 345–352.